# Solid-State Lasers for Coherent Communication and Remote Sensing

NASA Grant NAGW-1760

Semi-Annual Progress Report
for the period
April 1,1990 through September, 1990

Robert L. Byer
Principal Investigator

Edward L. Ginzton Laboratory
Stanford University
Stanford, California 94305

February, 1991

**Solid-State Lasers for Coherent Communication and Remote Sensing**

NASA Grant NAGW-1760

Robert L. Byer
Applied Physics Department
Stanford University
Stanford, California 94305

## ABSTRACT

Work in the stabilization of monolithic Nd:YAG lasers and the application of these lasers to nonlinear optical frequency conversion is discussed. The intrinsic stability of semiconductor-diode-laser-pumped solid-state lasers has facilitated a number of demonstrations in external resonant cavity harmonic generation and stable optical parametric oscillation. Relative laser frequency stabilization of 0.3 Hz has been achieved, and absolute stability of a few hundred hertz is anticipated. The challenge is now to reproduce this frequency stability in the output of tunable nonlinear optical devices. Theoretical and experimental work toward this goal are continuing.

**Solid-State Lasers for Coherent Communication and Remote Sensing**

NASA Grant NAGW-1760

Table of Contents

**Solid-State Lasers for Coherent Communication and Remote Sensing**

NASA Grant NAGW-1760

Personnel Associated with the Program

Robert L. Byer — Principal Investigator

Robert C. Eckardt — Senior Research Associate

Martin M. Fejer — Assistant Professor of Applied Physics

Eric Gustafson — Research Associate

Nick Sampas — Post Doctoral Research Affiliate

Timothy Day — Ph.D., September 1990

Steven T. Yang — Graduate Student

Christopher Pohalski — Graduate Student

Darwin Serkland — Graduate Student

# Solid-State Lasers for Coherent Communication and Remote Sensing

Robert L. Byer
Principal Investigator

## I Introduction

This progress report is presented in the form of two manuscripts that have been submitted for publication. The first manuscript describes a presentation given in Vilnius, Lithuania in August of 1990. Our work in the development and frequency stabilization of semiconductor-diode-laser-pumped solid-state lasers was presented. Emphasis was placed on research in nonlinear optical frequency conversion made possible through the use of these lasers to generate pump radiation for the nonlinear optical devices. These lasers are now being stabilized to better than one hertz relative to a high-finesse resonant cavity. Preliminary demonstrations have shown the possibility absolute stabilization to a few hundred hertz using sub-Doppler spectroscopy techniques with molecular absorptions in iodine.

The second manuscript describes a theoretical analysis of the tuning properties of monolithic doubly resonant optical parametric oscillators (DRO's). This paper will be published in the March issue of the Journal of the Optical Society of America B. The tuning properties of the DRO's are complicated, and stable operation requires that an number of critical tolerances be met. Monlithic DRO's that we have operated have displayed extremely good coherence properties, low thresholds (10 mW) for cw parametric oscillation, and good conversion efficiency. The potential of optical parametric oscillators for optical communication, remote sensing. spectroscopy, and even projection displays is extensive. This potential for application proves the motivation for stabilizing the DRO.

We are currently pursuing a number of projects in these areas. Work on both improved relative laser frequency stabilization and absolute stabilization is continuing. The single-mode output-power of our injection-locked Nd:YAG laser has recently been upgraded to 18 W, and cw harmonic generation has be demonstrated at 6.5-W power levels. This is adequate power to pump even a single resonant optical parametric oscillator. In addition we will be studying cascaded harmonic generation to the ultraviolet and a number of additional DRO and SRO schemes.

# Frequency Stable Operation of Nd:YAG Lasers

R. C. Eckardt, T. Day, E. K. Gustafson and R. L. Byer

Ginzton Laboratory
Stanford University
Stanford, California
94305-4085 USA

Abstract

Semiconductor-diode-laser-pumped solid-state lasers are inherently frequency stable when compared with other lasers, and this stability can be improved by active feedback control. Monolithic nonplanar ring oscillators constructed from solid pieces of the laser material provide better than 10-kHz frequency stability over 0.1-sec intervals. Active feedback stabilization of the cavity length has been used to demonstrate 0.3-Hz stabilization relative to a reference cavity resonance frequency. This range of frequency stability has application in nonlinear optical frequency conversion.

Resonantly enhanced nonlinear frequency conversion techniques, such as external-resonant-cavity harmonic generation and optical parametric oscillation, are particularly sensitive to the frequency stability of the pump radiation. High stability diode-laser-pumped solid-state lasers permit efficient cw second-harmonic generation (SHG) and optical parametric oscillation (OPO). An interesting aspect of this work is an analysis of the conditions required to produce single-mode-pair optical parametric oscillation. The exceptional frequency stability of the diode-pumped NonPlanar Ring Oscillator (NPRO) compared to dye lasers, gas lasers, or semiconductor lasers also provides some unique advantages for active frequency stabilization. Sub-Hertz relative frequency stability has been achieved by locking to reference cavities, and absolute stability of a few hundred Hz by locking to molecular or atomic absorptions appears possible.

Remeasurement of some nonlinear optical coefficients is a by-product that grew out of this work when it was found that some of the accepted values were predicting results that were inconsistent with experimental observations.

## 1. The NonPlanar Ring Oscillator

The solid-state monolithic NPRO[1,2,3] generates stable single-axial-mode output which is important for resonant cavity nonlinear optical frequency conversion. Semiconductor-diode-laser pumping of the NPRO's[4,2] provides advantages of efficiency and reduced heat loading. In addition, the low amplitude fluctuations of the diode-laser pump source provide improved frequency stability.

A schematic illustration of a NPRO is shown in Fig. 1. Spatial hole burning in the population inversion is avoided by unidirectional oscillation in a ring cavity which is important for single frequency oscillation. The monolithic cavity non-planar path includes three total internal

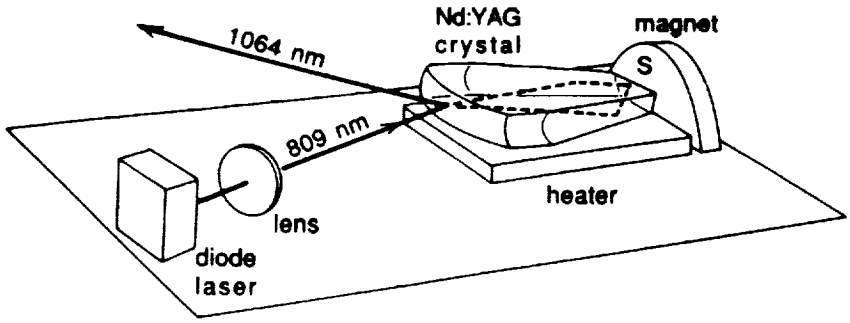


Fig. 1. Semiconductor-diode-laser-pumped Non-Planar Ring Oscillator (NPRO).

reflections and a fourth reflection at non-normal incidence from a multilayer-dielectric-coated curved output coupler. The total internal reflections provide reciprocal polarization rotation, and non-reciprocal rotation is produced by Faraday rotation when the laser material is placed in a magnetic field. The result is four nearly degenerate modes, two for the different eigen polarizations in each direction of oscillation. One of the four modes will have minimum loss.[3] Relatively small loss differences result in single-mode unidirectional laser oscillation. Designs have been produced that maximize loss difference to increase the resistance to optical feedback, an effect that can reduce frequency stability.[5]

The beatnote linewidth of monolithic Nd:YAG (neodymium-doped yttrium aluminum garnet) and Nd:GGG (neodymium-doped gadolinium gallium garnet) lasers has been observed to be between 3 kHz and 10 kHz for short periods of time, typically 100 ms.[6,4,7] Over longer periods of time the frequency drifts through greater excursions due to the temperature tuning rate which is -3.1 GHz/°C for monolithic Nd:YAG oscillators. Temperature fluctuations in the millidegree range produce a frequency wander of several MHz. Short term stability of a few kHz and MHz stability over periods of minutes, however, is adequate for a number of resonant cavity nonlinear frequency conversion demonstrations. And long term experiments can be carried out when the laser is slaved to the nonlinear cavity by active frequency control. The temperature sensitivity can be used for tuning, but the response is slow, typically 1 sec. Piezoelectric crystals bonded directly to non optical surfaces of the monolithic lasers provide limited tuning range but much faster response extending to frequencies of hundreds of kHz.[8,9] A split servo with feedback to both the temperature and the piezoelectric crystal can have both narrow jitter linewidth and long term frequency control.

## 2. Pulsed Applications

Pulsed pumping of monolithic lasers usually results in a frequency chirp during laser output caused by heating. Continuously pumped lasers reach a steady-state condition with constant temperature. However, the continuous wave output can be used to injection seed high-power pulsed lasers, or the cw laser output can be time gated and amplified. Another way in which

stable-frequency, pulsed operation is obtained from the monolithic lasers is by applying a small amount of modulation to the pump radiation at the relaxation oscillation frequency to produce spiking in the laser output. Each of these methods has been used to generate pulsed pump radiation for optical parametric oscillators, and the results of these investigations provide a heuristic review of the requirement for achieving single mode-pair oscillation of OPO's.

*a. Injection seeded Q-switched laser operation*

High-power Q-switched lasers have been a traditional source of pump radiation for singly resonant OPO's (SRO's). The short buildup times and high gain of the Q-switched lasers usually result in highly multimode output. If the oscillation of one mode is injection seeded with a few mW of cw radiation, oscillation on that laser mode can buildup and deplete the population inversion before other laser modes have a chance to grow to significant levels. Several commercial lasers are available that offer injection-seeded operation with nearly time-bandwidth-limited output of typically 10-nsec duration.

SRO's have been forced to operate resonated, single-mode signal even with highly multimode pumping.[10] The combined frequency selection of phase matching, a dispersing grating, and an intracavity etalon were necessary. The multi-axial-mode pump resulted in a multimode output at the nonresonated idler field. When this type of frequency control is used with a pulse SRO pumped with an injection-seeded Q-switched laser, the result is single-mode output at both the signal and idler wavelengths.[11] With the addition of piezoelectric control of the cavity length and computer control of all the adjustable parameters, spectrographic measurements with 300-MHz resolution were possible.[12] These SRO's used angle tuned $LiNbO_3$ pumped at 1.06 μm.

The single-mode pump alone is not sufficient to produce single-mode-pair oscillation in a simple SRO with no frequency selection except that of phase matching. This was observed in a $BaB_2O_4$ SRO pumped with the 354-nm third harmonic of the output of an injection seeded Q-switched Nd:YAG laser.[13] The single frequency pump did reduce OPO output energy fluctuation to 10% from 30% which was observed with multimode pumping when injection seeding of the Q-switched laser was blocked. The plane-parallel-cavity SRO with 1.2-cm-long $BaB_2O_4$ crystal and 3-cm overall length pumped by a 6-nsec pulse would oscillate on typically 8 axial modes at the signal wave. The broad tuning range of the $BaB_2O_4$ OPO extending from 412 nm to 2.55 μm included both the 1.064-μm fundamental and 532-nm second harmonic of the laser, which were available for injection seeding the SRO. With seeding, the buildup time of the SRO oscillation was substantially decreased, and single-mode-pair oscillated was achieved. Measurements of the SRO threshold yielded values that were less than predicted from calculations based on reported values of the nonlinear coefficient of $BaB_2O_4$. This lead to a reassessment of the scale for optical nonlinear coefficients.

*b. Nonlinear optical coefficient measurements*

The injection-seeded spatially-filtered Q-switched Nd:YAG laser provided a suitable pump for phase-matched second-harmonic measurements of the nonlinear optical coefficient. High optical

quality in both the pump beam and the nonlinear material is needed for precise control of phase matching which is also a requirement of these measurements. The measurements included careful characterization of phase matching for each observation. In addition it was determined that there were no extraneous spatial, temporal, or spectral components of the pump.

The results of careful nonlinear optical coefficient measurements[14] are reproduced in Table I. The investigation, which at first was motivated by the $BaB_2O_4$ SRO results, grew to include a total of six materials. This was necessary because the earlier $BaB_2O_4$ measurements were relative to KDP, and a controversy exists over the value of the nonlinear coefficient of that material. The measurements described here were performed in a two-beam setup which permitted both relative measurements between two crystal and absolute measurements with harmonic power measured in one beam and fundamental power measured in the other. The reproducibility of these measurements was ±4% which should also be the relative accuracy. The absolute accuracy is estimated to be better than ±10%.

The KDP coefficient listed in Table I agrees within experimental error with other phase-matched harmonic measurements.[15] The coefficients tabulated here yield a ratio $d_{22}(BaB_2O_4)/d_{36}(KDP)$ of 5.8 at variance with the ratio of 4.1 reported earlier. The absolute value for the $BaB_2O_4$ coefficient, however, more closely agrees with the SRO threshold observations. A more significant variance is with earlier parametric fluorescence measurement of $LiIO_3$ for which the nonlinear coefficient was 1.73 times the value reported here. Relative measurements between KDP and $LiIO_3$, however, are in agreement with earlier results. The difference between the previously reported nonlinear coefficient of KTP and that reported here is even larger: $d_{eff}$ = 7.3 pm/V reported earlier compared to 3.18 pm/V reported here. It is possible that some of these differences are due to sample to sample variations of the materials. Confirmation will come from application of these values. The highly coherent laser output that is becoming routinely available from diode-pumped solid-state lasers allows greater precision in the determination of nonlinear optical coefficients.

**TABLE I**
NONLINEAR OPTICAL COEFFICIENTS

| Crystal | Nonlinear optical coefficient[(a)] ($10^{-12}$ m/V) |
|---|---|
| KDP | $d_{36} = 0.38$ |
| KD*P | $d_{36} = 0.37$ |
| $LiIO_3$ | $d_{31} = -4.1$ |
| 5%MgO:$LiNbO_3$ | $d_{31} = -4.7$ |
| $BaB_2O_4$ | $d_{eff} = 1.94$ |
| | $\lvert d_{22}\rvert = 2.2$[(b)] |
| KTP | $d_{eff} = 3.18$ |
| | $\lvert d_{15}\rvert = 2.6$[(c)] |
| | $\lvert d_{24}\rvert = 3.3$ |

(a) Nonlinear coefficients are given for 1064- to 532-nm second-harmonic generation.
(b) Assumes that $\lvert d_{31}\rvert \ll \lvert d_{22}\rvert$ for $BaB_2O_4$.
(c) Using $\lvert d_{24}\rvert / \lvert d_{15}\rvert = 1.25$ and assuming $d_{24}$ and $d_{15}$ have the same sign.

*c. Long-pulse-pumped SROs*

Greater frequency selection is possible with longer buildup times to parametric oscillation. Pump pulses of 500-nsec duration were derived from a diode-pumped NPRO by gating the cw output followed by multipass amplification in a flashlamp pumped laser amplifier.[16] A monolithic SRO was pumped by the second harmonic generated by the oscillator-amplifier laser system. Pumping with the 532-nm harmonic allowed noncritical phase matching in the 5%MgO:$LiNbO_3$ crystal. The purpose of this experiment was to investigate spectral narrowing and to reduce OPO threshold to a level approaching that which could be achieved directly by diode-pumped lasers.

The monolithic SRO tuned from 834 to 958 nm and 1.47 to 1.2 μm when temperature was adjusted between 190° and 125°C.[17] Damage limitation of the MgO:$LiNbO_3$ SHG crystal required that the 5-kW output of the laser amplifier be no longer than 500 ns. Under these conditions 800 W of 532-nm harmonic was generated. The ring-cavity configuration of the SRO allowed high efficiency; up to 60% pump depletion was observed after threshold was reached. About 20% of the time single-mode operation of the SRO was observed. More often, however, simultaneous oscillation on three axial modes was observed, and occasionally as many as 8 modes oscillated simultaneously. Thus long-buildup time alone was not sufficient to guarantee single-mode oscillation.

*d. Doubly resonant optical parametric oscillation.*

A further reduction in OPO threshold is obtained with the doubly resonant oscillator (DRO) configuration in which the OPO is resonant at both the signal and idler wavelengths. The added constraint of double resonance in addition to phase matching and conservation of energy, however, makes stable operation of the DRO difficult.[18] The frequency stability of the NPRO and the mechanical stability of monolithic DRO construction are useful in overcoming this difficulty. A doubly resonant monolithic DRO was constructed from MgO:$LiNbO_3$ with broad-band dielectric mirrors highly reflecting near 1.06 μm coated on the crystal.[19] A ring geometry was formed by using reflections from two 10-mm radius-of curvature surfaces on the ends of the noncritically phase-matched, 1.25-cm-long crystal and a polished flat on one side for total internal reflection. The DRO was pumped at 532 nm by second-harmonic pulses generated from the relaxation oscillations of a Nd:YAG NPRO. Pulsed operation was required because the DRO threshold was marginally higher than could be produced by the NPRO and harmonic generator when operated cw.

A 10% modulation of the diode-laser current at 325 kHz drove the Nd:YAG NPRO into relaxation oscillations. The 1.06-μm fundamental pulses had 260-mW peak power and were efficiently converted into 400-ns, 230-mW, 532-nm pulses by externally resonant second-harmonic generation. The buildup of parametric oscillation occupied most of the pump pulse duration. Overall DRO efficiency was only 7% due to the long buildup time. After threshold was reached 60% pump depletion occurred. The DRO tuned between 1.02 and 1.12 μm by adjustment of both temperature and electric field. The most remarkable aspect of the DRO operation was that single-mode-pair oscillation was achieved on almost every pulse. The only

exception was when the DRO was tuned between cluster centers and either simultaneous or alternating output on widely spaced modes approximately 4 nm apart were observed. The monolithic DRO with a pulsed single-mode pump will oscillate on a single mode pair due to the constraint of double cavity resonance.

## 3. cw Applications

Continuous wave operation is important for narrow-bandwidth nonlinear optical frequency conversion. Transient conditions can be avoided with cw operation; even the time-bandwidth limitations of the pulsed applications described above exceed the short term frequency stability of diode-pumped solid-state lasers. Resonant-cavity techniques allow high-efficiency nonlinear optical frequency conversion at the power levels available from frequency stabilized diode-pumped solid-state lasers. The use of resonant cavities external to the the lasers simplifies the operation of the laser, but the laser and external cavity resonances must be locked together. Stable and efficient second-harmonic generation has been achieved with feedback control of the cavity resonance, and it should be possible to stabilize optical parametric oscillation with similar techniques.

*a. External resonant cavity harmonic generation*

The use of resonant-cavity harmonic generation external to the laser[20] allows the problems of laser stabilization and harmonic generation to be treated independently while high conversion efficiency is maintained. Second harmonic generation with only the fundamental resonated has been demonstrated using diode-pumped solid-state lasers.[21] It is possible to resonate both fundamental and harmonic,[22] but with double resonance care is required to preserve the phase relationship between fundamental and harmonic.[23] There are several methods that can be used to lock the fundamental frequency and the harmonic-generation resonant cavity. One of the simplest is the dither and lock technique. On resonance the reflected fundamental power is minimum. The optical length of the cavity can be modulated using either electro-optical or piezoelectric techniques or the frequency of the fundamental radiation can be modulated. An error signal is developed using phase sensitive detection of the reflected fundamental power. Using this technique, Kozlovsky, *et al.*[21] were able to generate 29.6 mW of cw 532-nm radiation from 56 mW of incident fundamental in a monolithic externally-resonant MgO:$LiNbO_3$ harmonic generator.

*b. cw pumped DRO*

A second monolithic MgO:$LiNbO_3$ DRO with higher finesse was prepared which could be pumped with the available cw 532-nm radiation.[24] This OPO had an observed cw threshold of 12 mW, and single-mode-pair oscillation was again observed. Temperature and electric-field tuning were used to tune the output from 1007 to 1129 nm. Dither and lock techniques were used to stabilize the DRO on a single mode-pair but only with limited success. The DRO would track frequency tuning of the pump for about 90 MHz. Pump depletion of 78% was observed at two times above threshold.

Measurements of the coherence properties[25] of this DRO demonstrated that the coherence of the pump was reproduced in the DRO output with little additional frequency noise. Furthermore, the sum of the phases of the signal and idler followed the phase of the pump. At degeneracy the DRO output was locked in phase with the pump laser output. It was not possible to use active control to stabilize the DRO for these measurements, perhaps due to shielding effects caused by trapped charges in the $MgO:LiNbO_3$. Instead, the DRO was temperature stabilized. It could be operated for 20 minutes at degeneracy and for about one minute on a mode-pair off degeneracy without a mode hop; this is long enough for measurements of coherence and to indicate the potential for active stabilization.

*c. Injection locking.*

The use of a low power frequency-stabilized oscillator to stabilize the output of a higher power oscillator is an established technique. When injecting the low-power master laser output into the higher power slave laser, it is necessary to isolate the master from optical feedback, provide spatial mode matching, and to lock the resonances of the master and slave lasers. High-power, diode-pumped lasers are in the developmental stage, but injection locking has been demonstrated on a hybrid system with a diode-pump laser used to lock the output of an arc-lamp-pumped, high-power laser.[26] Ring geometry was used in the high-power laser to reduced optical feedback and avoided spatial hole burning effects. Locking of the cavities was achieved by the FM-sideband technique which provided an error signal used to drive mirrors mounted on piezoelectric translators and control the cavity length of the slave oscillator. It was possible to maintain injection locking for a slave-to-master power ratio of 400:1 with a 13-W, single-frequency output. Analysis of phase noise showed the total additional rms phase noise of the slave over that present on the master oscillator was less than 0.3 radians. The measurement was limited by low-frequency laboratory acoustics. As the cost of semiconductor diode lasers decreases with advances in production, diode-pumped, high-power, solid-state lasers will become common.[27] A diode-pumped slave laser is expected to be much less noisy due to the more stable pumping provided by diode lasers, higher efficiency and therefore less heating, and the elimination of turbulent coolant flow. Such all-solid-state lasers are good candidates to scale the output of frequency stabilized lasers to higher powers.

## 4. Nd:YAG Laser Frequency Stabilization

It may be helpful to begin the discussion of frequency stabilization with the definition of terms and a mathematical overview. The specification of frequency noise uses quantities such as spectral bandwidth, linear spectral noise density, and Allen variance. It is often not possible to compare the laser to a more stable standard, and it becomes necessary compare two lasers with approximately the same level of frequency stability. If the two lasers are completely independent, the bandwidth of the difference frequency generated when the two laser outputs interfere at a photodetector, the heterodyne signal, sets an upper limit on the individual laser bandwidths. If the two lasers are not completely independent in such a comparison, it is possible that there will be some common mode rejection, that is some frequency noise will be identical in the two lasers

and not be evident in the heterodyne signal. Other measurements such as those derived from the signals used to stabilize a laser provide information on the lower bound of noise. Measurement by several different techniques reduce these uncertainties.

The spectral bandwidth is the frequency width that would be observed using a scanning interferometer with sufficiently narrow transmission band. The heterodyne signal of the laser output and a much more stable reference displaced from the laser output by a small frequency difference translates the laser spectral distribution to a region in which it can be measured by radio-frequency spectral analysis. Mathematically the bandwidth $\Delta f_{FWHM}$ is the full width at half maximum of the power spectrum,

$$W(f) = \frac{1}{2} E^{*}(f)\, E(f), \tag{1}$$

where $E(f)$ is defined by the Fourier transform

$$E(f) = \lim_{T \to \infty} \frac{1}{\sqrt{T}} \int_{-T/2}^{T/2} E(t)\, e^{i2\pi ft} dt. \tag{2}$$

The normalization of Eq. (2) is useful for ergodic processes. An ergotic process is one for which the time average is equal to the ensemble average. With this normalization, the power spectrum of an ergodic process will approach a constant distribution as the sample time $T$ increases.

The time dependent electric field of a phase modulated output can be expressed as

$$E(t) = E_o \exp\{-i\,[2\pi f_o t + \phi(t)]\}, \tag{3}$$

where $\phi(t)$ is a time dependent phase and $f_o$ is a fixed frequency. A phase noise can be represented by $\phi(t)$. The instantaneous frequency shift is given by

$$\Delta f(t) = \dot{\phi}(t) / 2\pi. \tag{4}$$

A complex spectral amplitude of frequency noise is obtained from the Fourier transform

$$S(f) = \frac{1}{\sqrt{T}} \int_{-T/2}^{T/2} \frac{\dot{\phi}(t)}{2\pi} e^{i2\pi ft}\, dt, \tag{5}$$

where $T$ is the duration of the sample. The linear spectral density of frequency noise is obtained by averaging the absolute value of the spectral amplitude over many samples

$$S_f(f) = \left\{ \langle S^{*}(f)\, S(f) \rangle \right\}^{1/2}. \tag{6}$$

The units of $S_f(f)$ are $\mathrm{Hz}/\sqrt{Hz}$. One method of measuring $S(f)$ is radio frequency analysis of a frequency discriminant signal, for example a voltage proportional to the instantaneous frequency shift of the laser output.

The Schawlow-Townes limit describes the noise due only to the random addition of spontaneous emission to the laser oscillation. The bandwidth of frequency noise in this limit is

$$\Delta f_{\mathrm{FWHM}} = 2\pi\Delta\nu_c^2 h\nu_l / P, \tag{7}$$

where $\Delta\nu_c$ is the width of the laser cavity resonance, $h$ is Planck's constant, $\nu_l$ is the frequency of the laser oscillation, and $P$ is the output power of the laser. The linear spectral density of frequency noise in the Schawlow-Townes limit is constant in frequency and given by

$$S_{f,0} = \Delta\nu_c\sqrt{2h\nu_l / P}. \tag{8}$$

The condition $(S_{f,0})^2 << B$ where $B$ is the bandwidth of the noise applies, and it is appropriate to use the relationship[28]

$$\Delta f_{\mathrm{FWHM}} = \pi S_{f,0}^2. \tag{9}$$

Another measure of frequency stability is the two sample variance

$$\sigma^2(\tau) = \frac{1}{2(M-1)}\sum_{i=1}^{M-1}(y_{i+1} - y_i)^2. \tag{10}$$

Here $y_i$ is the $i^{\mathrm{th}}$ frequency measurement of $M$ successive measurements each of duration $\tau$. A division of the two sample variance by the frequency of the oscillation yields the Allen variance.[29] In practice the two-sample variance can be measured using the heterodyne signal obtained from two lasers slightly offset in frequency. A time and interval counter can be used to measure zero crossings of the heterodyne signal in successive time intervals. One data set can be manipulated mathematically to yield the variance as a function of individual measurement duration.

*a. Laser stabilization loop*

The control loop for laser stabilization can be modeled as four elements: the laser oscillator which is perturbed by a noise process $S_{f,\mathrm{laser}}$, a discriminator that monitors the frequency fluctuations with a voltage responsivity $D_v$ in units of V/Hz, a servo that amplifies the error signal with a gain $G$, and an actuator that converts the amplified error signal to changes in laser frequency with the coefficient $K$ in units of Hz/V. Any stage may limit stabilization, but the discriminator is particularly susceptible to noise in the optical signal and technical noise such as length fluctuations of the reference cavity.

Diode-pumped, solid-state, monolithic lasers usually operate at the Schawlow-Townes limit of frequency stability above 50 kHz, and exhibit a noise roughly proportional to $1/f$ below that frequency. A piezoelectric crystal can be bonded to the monolithic laser oscillator to serve as the frequency actuator. A typical response coefficient for this type of actuator is $K = 1$ MHz/V with a ±20-MHz dynamic range and bandwidths flat to 200 kHz. Slower control of laser frequency with much larger range is achieved by temperature tuning. The servo has large gain at low frequencies, typically 120 dB, to control the large $1/f$ noise and unity gain in the 50- to 100-kHz

region. The discriminator technique that will be described here is called Pound-Drever[30] locking, which uses the reflection of a frequency-modulated signal from a reference cavity. Ideally the linear spectral density of frequency noise $S_{f,cl}$ under closed-loop conditions would be reduced from the free running value for the laser by

$$S_{f,cl} = \frac{S_{f,laser}}{|1 + K G D_v|}, \tag{11}$$

where $K$ is the actuator response coefficient, $S$ is the servo gain, and $D_v$ is the discriminator voltage responsivity. If stabilization is limited by noise in the frequency discriminant, the minimum linear spectral noise density will be

$$S_{f,cl,min} = \frac{S_{f,disc}}{D_v}. \tag{12}$$

*b. Frequency discriminant*

Resonant cavities can be used for a stabilization reference both in transmission and reflection. The frequency modulation technique using reflection proposed by Drever, *et. al* [30] has several advantages over locking to the side of a cavity transmission band. A frequency modulation is applied to the laser output before it is incident on the reference cavity. The modulation frequency is typically 10 MHz or greater. The FM side bands are separated from the carrier by the modulation frequency which is greater than the optical bandwidth of the reference cavity. If the carrier is centered on the resonance it will be at a minimum of reflection, and if the carrier is slightly detuned from resonance, the amplitude of its reflection will grow, and it will be shifted in phase by an amount dependent on the detuning. The FM sidebands, however, will be well separated from the cavity resonance and therefore be nearly totally reflected with no phase change. The reflected light has a resulting amplitude modulation which is dependent in magnitude and sign of the degree of detuning of the carrier. The modulation frequency of the AM signal is the same as that of the FM.

In the simplest analysis an FM signal can be approximated by a carrier and two sidebands

$$\begin{aligned} &\sin\{\omega_o t + \alpha + \beta \sin(\omega_m t + \gamma)\} \\ &\approx \sin(\omega_o t + \alpha) + \frac{\beta}{2}\sin[(\omega_o+\omega_m)t+\alpha+\beta] + \sin[(\omega_o-\omega_m)t+\alpha-\beta+\pi]\,. \end{aligned} \tag{13}$$

Note that the sum of the phases of the two sidebands differs by $\pi$ from twice the phase of the carrier. A similar expansion illustrates that the sum of the phases of AM sidebands is exactly twice the phase of the carrier. More accurately the FM signal is represented by a series with Bessel function coefficients

$$\exp\{i(\omega_o t + \beta \sin \omega_m t)\} = \left[J_0(\beta) + \sum_{k=1}^{\infty} J_k(\beta)\left\{e^{ik\omega_m t} + (-1)^k e^{-ik\omega_m t}\right\}\right] e^{i\omega_o t}. \quad (14)$$

The complex reflection coefficient of the resonator is

$$R(\Delta f) = \frac{r_1 - r_2 e^{i\theta(\Delta f)}}{1 - r_1 r_2 e^{i\theta(\Delta f)}}, \quad (15)$$

where $r_1$ and $r_2$ are the field reflection coefficients of the first and second mirrors respectively and the cavity round trip phase shift is given by $\theta(\Delta f) = 2\pi \Delta f / \Delta f_{FSR}$ where $\Delta f_{FSR}$ is the free spectral range of the reference cavity. Eq. (15) assumes there are no losses in the cavity. If $r_1 = r_2 = r$, and $\Delta f$ is small compared to $\Delta f_{FSR}$, then

$$R(\Delta f) \approx \frac{-i\theta(\Delta f)}{1 - r^2} \approx \frac{-i 2\mathcal{F}\Delta f}{\Delta f_{FSR}}, \quad (16)$$

where $\mathcal{F}$ is the finesse of the resonator. If the reflectivity given by (16) is assigned to the carrier of (13) and the two side bands are assigned unity reflectivity, the total reflected intensity is obtained by taking the square of the absolute value of the amplitude. Only the term that is intensity modulated at angular frequency $\omega_m$ is kept, and this result is normalized by dividing by the average value of the incident intensity to yield the normalized error signal

$$V_{NOR} = \frac{I_r(\omega_m)}{I_i} = -(4\beta F \Delta f / \Delta f_{FSR}) \sin \omega_m t. \quad (17)$$

This result is in agreement with a more detailed derivation[31] that treats a single Fourier component of frequency noise rather than a fixed frequency offset and uses Eqs. (14) and (15) in the expansion. The detailed derivation uses an incident field that is modulated at two frequencies

$$E = E_i \exp\{i(\omega_o t + \alpha \sin \omega_N t + \beta \sin \omega_m t)\}, \quad (18)$$

with the conditions that $\omega_o >> \omega_m >> \omega_N$ and $\alpha << 1$. The normalized signal is

$$V_{NOR} = \frac{8\mathcal{F}}{\Delta f_{FSR}} J_o(\beta) J_1(\beta) \sqrt{\frac{\mathrm{sinc}^2(x_N/G)}{1 + G^2 \sin^2(x_N/G)}}\, \alpha f_N \cos(\omega_N t + \phi) \sin \omega_m t, \quad (19)$$

where $x_N = \frac{2f_N}{\Delta f_{FSR}}$, $G = 2\mathcal{F}/\pi$, and $\tan\phi = -G \tan(x_N / G)$. The added detail of Eq. gives information about the frequency response of the frequency discriminant. Bandwidth, frequency dependent phase shift, and optimum value for the depth of modulation $\beta = 1.08$ are specified by this equation.

The FM stabilization technique offers several advantages over the transmission method of stabilization. The error signal for the FM technique is at a frequency well above the frequency of excess noise amplitude fluctuations of the laser over the shot noise limit, thus preventing these amplitude fluctuations from being interpreted as frequency noise. Also the FM technique does not have loop delays due to resonance buildup time, and it has a slightly greater sensitivity to frequency change than the transmission method.

*c. Laser frequency noise*

It is important to characterize the spectral density of frequency noise of the laser for the purpose of determining design parameters of the control loop. The frequency discriminant is useful for this measurement. Calibration of the frequency discriminant was performed by directing the laser output through an acousto-optic modulator in addition to the electro-optical modulator that was introducing the 10-MHz FM sidebands. The frequency of the acousto-optic modulator was in turn modulated with a low frequency sinusoidal input. The fixed frequency offset of the deflected beam had no consequence, but the varying component served as a calibrated frequency noise signal. The total modulation of the laser output was as described in Eq. (18). The measurement of laser spectral noise density was performed under closed loop conditions, and the laser noise was deconvolved with knowledge of the characteristics of the loop components. This measurement was performed using a 40-mW commercial Nd:YAG NPRO. The results[31] are shown in Fig. 2. Similar results have been obtained with various techniques such as Fourier analysis of time domain measurements, fiber delay measurements,[32] and cavity transmission measurements.[33]

The spectral noise density of the Nd:YAG NPRO has a strong $1/f$ dependence decreasing to a constant value at approximately 50 kHz. The white noise above 50 kHz is approximately four times the calculated Schawlow-Townes limit of 0.05 Hz $/\sqrt{\text{Hz}}$. The observed noise density at 1 kHz is 20 Hz $/\sqrt{\text{Hz}}$. Corresponding values at this frequency are typically $10^3$ Hz $/\sqrt{\text{Hz}}$ for dye lasers and nearly $10^4$ Hz $/\sqrt{\text{Hz}}$ for Argon ion lasers. The noise of the NPRO appears largely due to fluctuations in the output of the diode pump laser used for pumping. This is substantiated by numerical modeling which shows that white noise in the diode-laser output would transfer to the spectral noise density with the same frequency dependence observed. If the diode laser noise were reduced to the shot noise limit, the numerical calculation indicates that the spectral noise density of the NPRO would

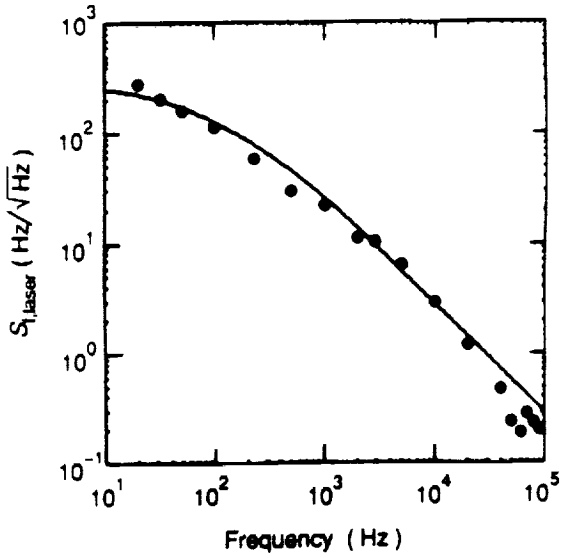


Fig. 2. Measured NPRO linear spectral density of frequency noise (data points) compared to the modeled frequency dependence for pump with a white noise component (solid line).

decrease to 20 Hz $/\sqrt{\text{Hz}}$ at DC. The low noise and potential for further noise reduction make the NPRO an excellent laser for frequency stabilization.

*d. Frequency stabilization of the NPRO*

The FM-stabilization or Pound-Drever technique was used to stabilize two identical NPRO lasers. The lasers were locked to adjacent fringes of a Fabry-Perot cavity with a finesse of $\mathcal{F}$ = 22,000 and a free spectral range of $\Delta f_{FSR}$ = 6.327 GHz. The frequency separation resulting from the use of adjacent fringes allowed independent stabilization of the two lasers relative to the same reference cavity. In this measurement[34,35] the two lasers were constructed from Nd:GGG which has a higher Verdet constant than Nd: YAG. The higher Verdet constant provided greater loss difference of the lasers modes and therefore higher resistance to optical feedback.

The experimental setup for the stabilization of the two lasers is shown in Fig. 3. The FM frequencies imposed by the two electro-optical modulators EO1 and EO2 were 10.9 and 20.3 MHz respectively. The two laser beams were combined at the beamsplitter (BS). One of the beams from the beamsplitter was incident on a fast photodiode (D1) used to observe the beating of the laser outputs at 6.327 GHz. This signal was mixed down to 20 kHz with a precision RF oscillator and analyzed with an audio spectrum analyzer. The second combined beam from the beamsplitter was transmitted through a polarizing beamsplitter (PBS), a quarter wave plate ($\lambda/4$), and a mode-matching lens (L1), then reflected from the reference cavity back through the lens and waveplate to the polarizing beam splitter where it was reflected to a second photodiode (D2). The signal from the photodiode was mixed with the 10.9- and 20.3-MHz signals from oscillators $f_1$ and $f_2$. The signals from the mixers were sent through respective low pass filters and amplified in the servos, and finally applied to the actuators piezoelectric crystals on the lasers. The actuator response was $K$ = 450 kHz/V with a bandwidth of 500 kHz and a 20-MHz dynamic range. The servos had 125-dB gain at DC and unity gain at 100 kHz. The discriminant response was 0.4 V/MHz.

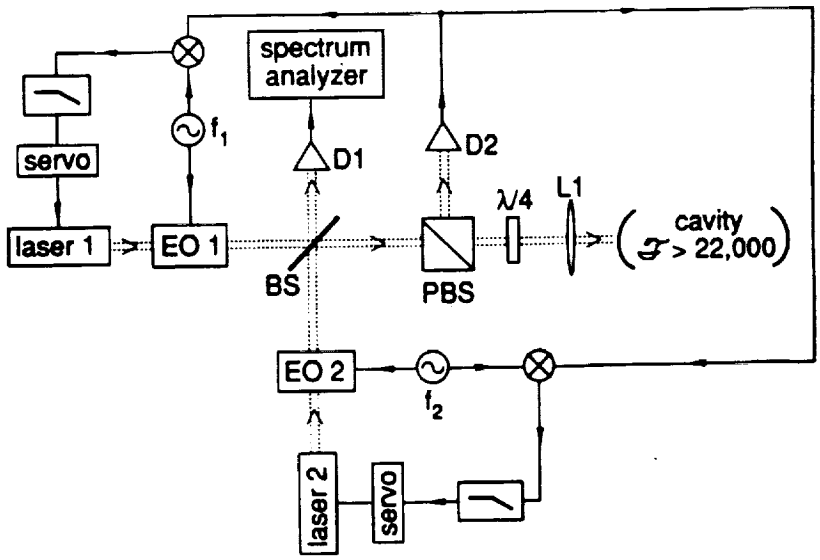


Fig. 3. Schematic diagram of dual-laser locking system.

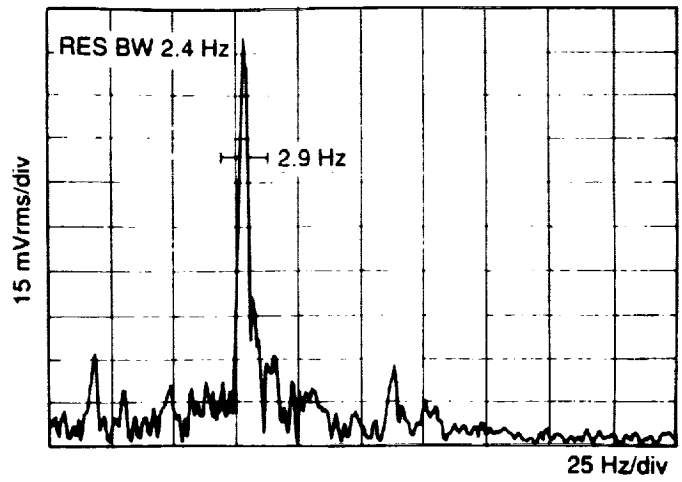


Fig. 4. Radio-frequency spectral analysis of heterodyne beat note between two stabilized NPRO's.

The beatnote bandwidth observed with the spectrum analyzer was 2.9 Hz (Fig. 4). Sampling times of 1.6 sec were used. Two-sample-variance measurements were also performed on the heterodyne signal from the two lasers (Fig. 5). The two-sample variance decreases with increased sample duration as typical of white noise until a minimum of 4.3 Hz was reached for $\tau$ = 0.2 sec. The increase after the minimum is typical of long-term drift. An analysis of the shot-noise limit of the discriminant signal shows that each laser has a theoretical noise bandwidth of

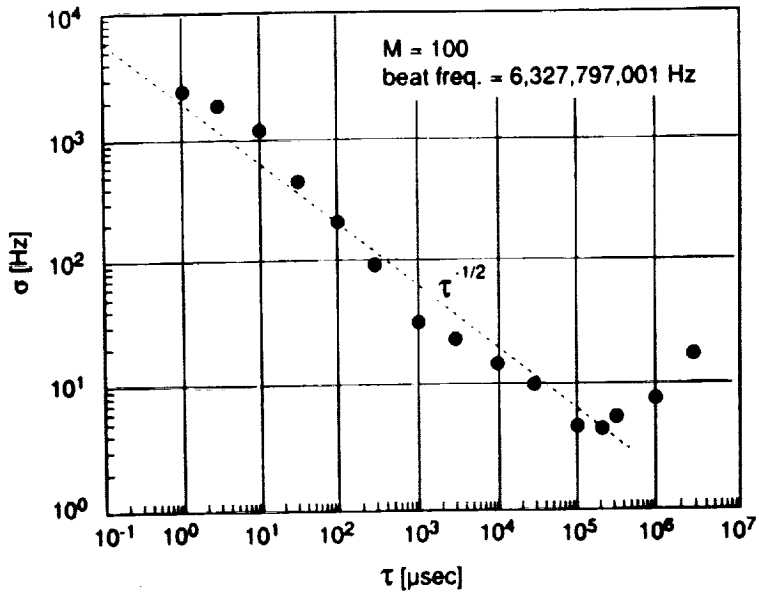


Fig. 5. Two-sample root variance of heterodyne beat note between two stabilized NPRO's.

2.2 Hz. All three of these values, 2.9-Hz beatnote, 4.3-Hz minimum two-sample variance, and calculated 2.2-Hz shot-noise-limited laser bandwidth are in reasonable agreement.

In a subsequent experiment[31] the heterodyne beatnote linewidth was reduced to 0.33 Hz. The main factor allowing this was an increase in laser output power. The 2-mW Nd:GGG lasers were replace with 40-mW Nd:YAG NPRO lasers. The increased power and increased sensitivity of the Nd:YAG lasers to feedback made additional isolation necessary. An acousto-optic modulator was used to shift the frequency of the lasers before reflection from the reference cavity. This in combination with the polarizing beam splitter and quarter wave plate provided the required degree of optical isolation. The increased power lowered the theoretical bandwidth due to shot noise to 21 mHz. However, another limit to stabilization had been reached. This limit appears to be mechanical or acoustic noise in the reference cavity. The excess noise of the reference cavity will change the free spectral range as well as the frequency of the resonances.

The work described above is on relative stabilization of the laser frequency. The absolute stabilization is only as good as that of the reference cavity. Work is continuing to isolate the reference interferometer from laboratory noise and to achieve stabilization with narrower reference cavity resonances. The necessity for stabilization of the reference cavity is well known.[36] Absolute stabilization of Nd:YAG lasers is possible by locking to atomic or molecular absorptions.[37] He-Ne lasers have been stabilized to 50-mHz levels.[36] Solid-state lasers have many properties important for frequency stable operation and may eventually be stabilized as well or better than He-Ne lasers.

## 5. Conclusion

Diode-pumped monolithic solid-state lasers have intrinsically narrow linewidths. The nonplanar ring geometry offers advantages of high-power, unidirectional, single-mode operation and greater resistance to optical feedback. The laser frequency can be tuned either slowly by temperature or rapidly with contacted piezoelectric transducers. These lasers have been used in applications of injection seeding high-peak-power pulsed lasers and injection locking high-power cw lasers. The improved coherence is important in nonlinear-optical frequency conversion. Stable externally resonant second-harmonic generation has been achieved using these lasers for the generation of pump radiation. The low-noise free-running NPRO lasers has been useful in pumping optical parametric oscillators allowing developments that were difficult or impossible in the past. The improved coherence is important in more traditional nonlinear optical applications and has resulted in a reevaluation of some nonlinear optical coefficients.

The noise properties of the diode-pumped NPRO lasers are suited to frequency stabilization applications. Relative stabilization to a reference cavity of 0.3 Hz has been demonstrated. There is now a challenge to reproduce this level of frequency stability in the output of an OPO at arbitrarily selected frequencies. Diode-pumped, monolithic, solid-state lasers have lower free running noise than other lasers and potential for higher levels of stabilization.

## References


1. T. J. Kane and R. L. Byer, Opt. Lett. **10**, p. 65, (1985).
2. W. R. Trutna Jr., D. K. Donald and M. Nazarathy, Opt. Lett. **12**, p. 248, (1987).
3. A. C. Nilsson, E. K. Gustafson and R. L. Byer, IEEE J. Quantum Electron. **25**, p. 767, (1989).
4. T. J. Kane, A. C. Nilsson and R. L. Byer, Opt. Lett. **12**, p. 175, (1987).
5. A. C. Nilsson, T. J. Kane and R. L. Byer, Proc. SPIE **912**, p. 13, (1988).
6. B.-K. Zhou, T. J. Kane, G. J. Dixon and R. L. Byer, Opt. Lett. **10**, p. 62, (1985).
7. W. K. Williams, A. Dandridge, A. D. Kersey, J. F. Weller, A. M. Yurek and A. B. Tveten, Electron. Lett. **25**, p. 774, (1989).
8. A. Owyoung and P. Esherick, Opt. Lett. **12**, p. 999, (1987).
9. T. J. Kane and E. A. P. Cheng, Opt. Lett. **13**, p. 970, (1988).
10. S. J. Brosnan and R. L. Byer, IEEE J. Quantum Electron. **QE-15**, p. 415, (1979).
11. T. K. Minton, S. A. Reid, H. L. Kim and J. D. McDonald, Opt. Commun. **69**, p. 289, (1989).
12. T. K. Minton, H. L. Kim, S. A. Reid and J. D. McDonald, J. Chem. Phys. **89**, p. 6550, (1988).
13. Y. X. Fan, R. C. Eckardt, R. L. Byer, J. Nolting and R. Wallenstein, Appl. Phys. Lett. **53**, p. 2014, (1988).
14. R. C. Eckardt, H. Masuda, Y. X. Fan and R. L. Byer, IEEE J. Quantum Electron. **26**, p. 922, (1990).
15. D. Eimerl, "Electro-optic, linear, and nonlinear optical properties of KDP and its isomorphs." 1987 **72**, p. 95, (1987).
16. T. J. Kane, W. J. Kozlovsky and R. L. Byer, Opt. Lett. **11**, p. 216, (1986).
17. W. J. Kozlovsky, E. K. Gustafson, R. C. Eckardt and R. L. Byer, Opt. Lett. **13**, p. 1102, (1988).
18. R. G. Smith, IEEE J. Quantum Electron. **QE-9**, pp. 530-540, (1973).
19. W. J. Kozlovsky, C. D. Nabors, R. C. Eckardt and R. L. Byer, Opt. Lett. **14**, p. 66, (1989).
20. A. Ashkin, G. D. Boyd and J. M. Dziedzic, IEEE J. Quantum Electron. **QE-2**, p. 109, (1966).
21. W. J. Kozlovsky, C. D. Nabors and R. L. Byer, IEEE J. Quantum Electron. **24**, p. 913, (1988).
22. C. Zimmermann, R. Kallenbach, T. W. Hänsch and J.Sanberg, *Opt. Comm.* **71**, 229, (1989).
23. L.-A. Wu and H. J. Kimble, *J. Opt. Soc. Am. B* **2**, 697, (1985).
24. C. D. Nabors, R. C. Eckardt, W. J. Kozlovsky and R. L. Byer, Opt. Lett. **14**, p. 1134, (1989).
25. C. D. Nabors, S. T. Yang, T. Day and R. L. Byer, J. Opt. Soc. Am. B **7**, p. 815, (1990).
26. C. D. Nabors, A. D. Farinas, T. Day, S. T. Yang, E. K. Gustafson and R. L. Byer, Opt. Lett. **14**, p. 1189, (1989).
27. R. L. Byer, Science **239**, p. 742, (1988).
28. D. S. Elliott, R. Roy and S. J. Smith, Phys. Rev. A **26**, p. 12, (1982).
29. D. W. Allen, IEEE Trans. Ultrson. **UFFC-34**, p. 647, (1987).
30. R. W. P. Drever, J. L. Hall, F. V. Kowalski, J. Hough, G. M. Ford, A. J. Munley and H. Ward, Appl. Phys. B. **31**, p. 97, (1983).
31. T. Day, "Frequency Stabilizated Solid State Lasers for Coherent Optical Communications," (Ph.D. thesis,Stanford University, Stanford, CA, 1990).
32. W. K. Williams, A. Dandridge, A. D. Kersey, J. F. Weller, A. M. Yurek and A. B. Tveten, Electron. Lett. **25**, p. 774, (1989).
33. P. Fritschel, A. Jeffries and T. J. Kane, Opt. Lett. **14**, p. 993, (1989).
34. T. Day, A. C. Nilsson, M. M. Fejer, A. D. Farinas, E. K. Gustafson, C. D. Nabors and R. L. Byer, Electron. Lett. **25**, p. 810, (1989).
35. T. Day, E. K. Gustafson and R. L. Byer, Opt. Lett. **14**, p. 221, (1990).
36. Ch. Salomon, D. Hill, and J. Hall, J. Opt. Soc. Am. B, **5**, 1576, (1988).
37. A. A. Mak and V. I. Ustyugov, Proc. SPIE **1132**, p. 58 (1989).

# Optical parametric oscillator frequency tuning and control

Robert C. Eckardt, C. D. Nabors,* William J. Kozlovsky,† and Robert L. Byer

*Edward L. Ginzton Laboratory, Stanford University, Stanford, California 94305-4085*

Received May 15, 1990; accepted August 7, 1990

The frequency-tuning and control properties of monolithic doubly resonant optical parametric oscillators are analyzed for stable single-mode pump radiation. Single-axial-mode operation is observed on the idler and the signal for both pulsed and continuous pumping. Projections are made for tuning-parameter tolerances that are required for maintenance of stable single-frequency oscillation. Continuous frequency tuning is possible through the simultaneous adjustment of two or three parameters; thus the synthesis of specific frequencies within the broad tuning range of the doubly resonant optical parametric oscillator is permitted.

## 1. INTRODUCTION

An analysis of the frequency-tuning properties of doubly resonant optical parametric oscillators (DRO's), based on both experimental observations and theoretical modeling, is presented. Specific details in this presentation of frequency control and synthesis apply to monolithic DRO's constructed from $LiNbO_3$. Where possible, however, results are given with more general applicability. The purpose is achievement of a quantitative understanding of the conditions required for stable single-axial-mode parametric oscillation and the resulting frequency stability of the DRO output. Approaches to frequency synthesis and continuous frequency tuning that are based on the simultaneous adjustment of two or three tuning variables are described.

The potential of optical parametric oscillators (OPO's) for the generation of tunable coherent radiation was recognized more than twenty-five years ago.[1] The complex tuning properties of DRO's were also revealed in early demonstrations and analyses.[2,3,4] Optical parametric oscillation has been discussed in detail in a number of reviews,[5,6,7] and it is a subject treated in more general terms in a number of books that discuss nonlinear optics.[8] Improvements in the quality of nonlinear-optical materials and in the coherence of pump sources led to a number of advances in the performance of OPO's. Using recent experimental results obtained with stable single-mode pump sources and monolithic DRO's constructed from high-quality $LiNbO_3$ nonlinear-optical material, we are able to apply and to extend the earlier analyses.

Resonance of both the signal and the idler frequencies, double resonance, offers the advantage of a lower threshold for parametric oscillation than in single resonance. Double resonance also provides additional frequency selectivity in OPO operation. These desirable properties of double resonance, however, come with a considerable increase in the complexity of tuning and with more restrictive tolerances on pump stability and cavity stability. Diode-pumped solid-state lasers provide the required pump-frequency stability, and monolithic cavities provide the required mechanical stability in the OPO. Continuous tuning is difficult in DRO's, which typically tune with axial mode hops and cluster jumps over hundreds of axial modes. Nevertheless, using improved pump sources and nonlinear-optical materials coupled with multiple-parameter control, DRO's can in principle be operated stably and tuned continuously, thus widening their range of applications.

DRO's can provide highly coherent output, reproducing the statistical properties of the pump with little additional noise. This was shown theoretically by Graham and Haken[9] in a quantum-mechanical analysis of the DRO, and it was demonstrated in experimental measurements of the coherence properties of the DRO. The quantum-mechanical analysis showed that the diffusion of the sum of the signal and the idler wave phases follows the phase diffusion of the pump wave adiabatically. Although the phase difference of the signal and the idler may diffuse in an undamped manner, the statistical properties of a DRO are basically the same as those of an ideal laser. A result of these properties is the addition of only a small amount of phase noise in the output of the DRO above that present in the pump. This has been confirmed in coherence measurements of the output of a cw DRO.[10] For periods of ~1 min, the free-running DRO that was not servo locked oscillated on a single mode pair without a mode hop. That the DRO did not add significant excess linewidth over that present on the pump was demonstrated with the measurement of beating between the DRO output and an independent diode-laser-pumped solid-state laser during the periods between mode hops. The beat-note linewidth was 13 kHz, which was the expected value for the typically 10-kHz linewidths of the pump laser and the independent reference laser. Additional coherence measurements showed that the signal and the idler were phase anticorrelated when referenced to the pump laser. Also, the width of the signal–idler beat note with the DRO near but not at degeneracy was less than 1 kHz. The signal–idler beat note indicates the frequency fluctuations added to the DRO output in addition to those present on the pump.

0740-3224/91/030000-00$02.00 

The results of the classical stationary analysis presented here are consistent with the earlier analyses and measurements. The main purpose of this presentation is explanation of the complex tuning properties of the DRO in order to permit fuller use of its remarkable coherence and spectral properties. The theoretical presentation of Section 2 begins in Subsection 2.A with a qualitative overview of DRO tuning. This overview is used to establish the extensive terminology required for the discussion. In Subsection 2.B the threshold condition for parametric oscillation is reviewed and recast in terms that are more easily adapted to tuning calculations. The theoretical basis of frequency selection is discussed in Subsection 2.C. Experimental tuning data is presented in Section 3. The degree to which our theoretical model describes the observed tuning justifies some confidence in its use for predictive calculations in Section 4. Results are summarized and discussed in Section 5. Finally, the properties of $MgO:LiNbO_3$ that are required for modeling the experimental data are reviewed in Appendix A.

## 2. THEORY

### A. DRO Tuning Overview

A nonlinear-optical material pumped by intense optical radiation at frequency $\omega_p$ can provide gain at two lower frequencies, called the signal and the idler and related by the conservation-of-energy condition

$$\omega_p = \omega_s + \omega_i . \tag{1}$$

The parametric interaction is phase dependent, and proper phasing is required for energy to flow from the from the pump field to the signal and the idler fields. Phase-velocity matching ensures that the relative phases of the three waves do not change with propagation through the nonlinear material. Phase matching is described by the wave-vector mismatch, which for the case of collinear propagation can be expressed by the scalar relationship

$$\Delta k = k_p - k_s - k_i = (n_p\omega_p - n_s\omega_s - n_i\omega_i)/c , \tag{2}$$

where $k_p$, $k_s$, and $k_i$ are the respective wave-vector magnitudes of the pump, the signal and the idler waves, with corresponding indices of refraction given by $n_p$, $n_s$, and $n_i$, and $c$ is the velocity of light. Useful parametric gain exists in the range of signal and idler frequencies for which $|\Delta k| \lesssim \pi/l$, where $l$ is the length of the nonlinear material. The parametric gain is maximum near $\Delta k = 0$. Phase matching is often achieved by controlling the birefringence of a nonlinear crystal through temperature or angle of propagation.

An OPO requires feedback at either (or both) the signal or the idler frequencies. If there is feedback at only one frequency, the device is called a singly resonant oscillator. Doubly resonant oscillators have feedback at both the signal and the idler frequencies. Feedback can be provided by placing the nonlinear material in a cavity formed by two external mirrors, or in the case of monolithic OPO's, highly reflecting coatings can be applied directly to the nonlinear material. Ring-cavity configurations offer the advantages of reduced feedback to the pump source and improved OPO conversion efficiency.[11] Figure 1 illustrates schematically several configurations for parametric

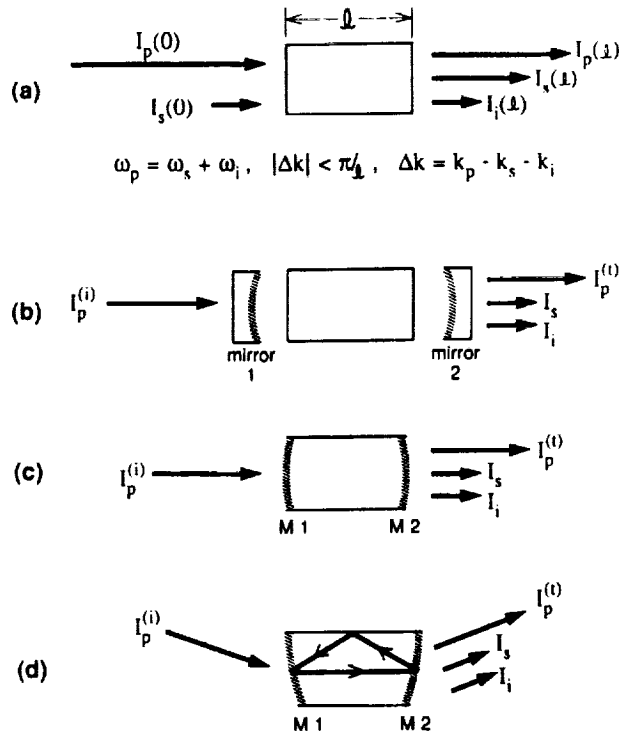


Fig. 1. (a) Schematic representation of optical parametric amplification. Optical parametric oscillators can be formed by the addition of mirrors that are separate from the nonlinear material, as shown in (b). Monolithic oscillators (c) and (d), with highly reflecting coatings (M's) applied directly to the nonlinear material, offer the advantages of low loss and rigidity that are important in stable, single-frequency DRO operation. Ring oscillators (d) offer the advantages of reduced feedback and improved conversion efficiency over standing-wave oscillators.

oscillators. Both standing-wave and ring-cavity monolithic DRO's were used for the experimental observations described in this paper. The tuning properties were quite similar, and the same model of tuning properties could be used for both, because the return path length differed little from the gain path in the ring resonators.

Phase matching is the major factor in determining broad tuning properties of an OPO, although cavity resonances have the major effect on details of frequency tuning. The conditions $\omega_p = \omega_s + \omega_i$ and $\Delta k = 0$ define phase-matching curves. The most commonly shown OPO phase-matching curve is the parabolalike shape for type-I phase matching in a birefringent crystal, for which the signal and the idler waves have the same polarization and the pump wave has the orthogonal polarization. Figure 2(a) shows a near-degeneracy ($\omega_s \sim \omega_i$) section of the temperature–tuning curve for a $LiNbO_3$ noncritically phase-matched OPO. Propagation is along a crystal principal axis in noncritical phase matching, which reduces dependence on propagation direction and eliminates birefringent walk-off.

The spectral width of the parametric gain is also determined by phase matching. A typical spectral distribution for single-pass gain at fixed temperature is shown in Fig. 2(b). Doubly resonant oscillation also entails simultaneous signal and idler resonance. Dispersion causes different cavity axial-mode frequency spacings for the two waves,

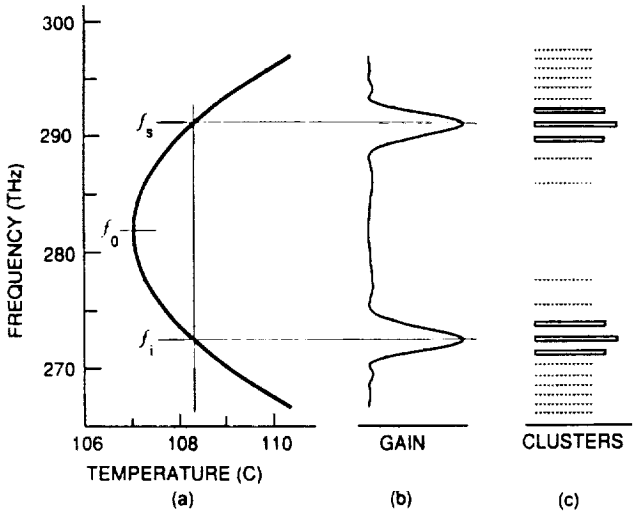


Fig. 2. (a) Typical OPO tuning curve near the degeneracy frequency $f_0 = f_p/2$, where $f_p$ is the pump frequency. The signal and the idler frequencies are shown for a $LiNbO_3$ OPO as a function of the tuning parameter, in this case temperature. For a fixed value of the tuning parameter, single-pass parametric gain exists in bands that are centered on the phase-matching wavelengths, as shown in (b). DRO's have the added constraint that the signal and the idler cavity resonances must coincide in satisfying the condition $f_p = f_s + f_i$, which results in output at cluster frequencies (c). Only two or three clusters, represented by open lines, are located within the gain bandwidth. Usually one cluster, represented by the longest open line, dominates.

and the simultaneous resonance condition thus occurs only at intervals in frequency. The regions of simultaneous resonance, called cluster frequencies, are indicated in Fig. 2(c). Early DRO's were observed to oscillate on a group or cluster of adjacent cavity axial modes. The wavelength of the cluster would at first shift continuously with tuning and then exhibit a discontinuous jump to another cluster of modes. The curves of Fig. 2 are intended to illustrate some general properties of the frequency tuning of DRO's. The curves were calculated for the 12.5-mm-long monolithic MgO:$LiNbO_3$ oscillators, pumped at 564 THz (532 nm), that are discussed in this paper.

A useful device for understanding the requirement for simultaneous cavity resonances is a type of diagram used by Giordmaine and Miller[2]; the cavity resonances near the oscillating signal and idler frequencies are plotted as a function of the respective frequencies, as shown schematically in Fig. 3. The difference between signal and idler axial mode spacings, $\delta\omega_s$ and $\delta\omega_i$, respectively, is exaggerated in this figure for the purpose of illustration. One frequency, here the signal, increases from left to right. The other frequency scale, the idler, is determined by the first scale and the conservation-of-energy condition in such a way that a vertical line drawn through the diagram will give signal and idler frequencies that satisfy Eq. (1). If a signal–idler resonance pair lie on a vertical line, they satisfy the simultaneous resonance condition. If the temperature or the dc electric field applied to the crystal is changed, the position of the resonances will advance along the scales, one to the left and the other to the right, at slightly different rates because of dispersion, but the scales will not change. If pump frequency is changed, the frequencies of the cavity resonances will not change, but one of the frequency scales will be displaced with respect to the other, and the respective resonances will move with that scale.

Two types of discontinuous frequency shifts are indicated in Fig. 3. One is an axial mode hop and the other is a cluster jump. As a tuning variable is changed, better coincidence in satisfying the conservation-of-energy condition is attained on adjacent signal and idler axial modes. It then becomes advantageous for the oscillation frequencies to hop to the adjacent modes, to one higher in frequency and the other lower. This type of discontinuous frequency change is referred to as a mode hop. Other factors such as phase matching also affect the selection of the oscillation frequencies. As the tuning variable changes, phase matching also changes, and at some point it is advantageous for the oscillator to jump to the next cluster. This is illustrated in the schematic tuning curve of Fig. 4. The signal or the idler oscillation frequency progresses along a cluster curve in a series of mode hops until another cluster curve more closely approaches phase matching. At that point the larger discontinuous frequency change of a cluster jump takes the oscillation to the next cluster curve. Figures 3 and 4 are only schematic, with dispersion greatly exaggerated. Typically there several hundred axial modes between adjacent cluster frequencies.

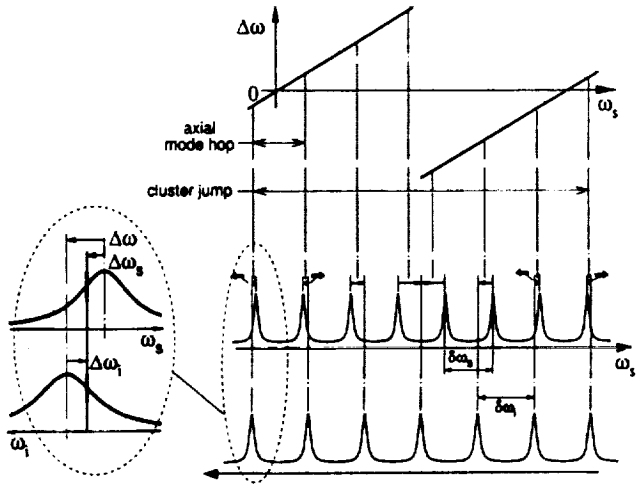


Fig. 3. Diagram[2] that shows the relationship between the DRO signal and idler resonance frequencies and the conservation-of-energy condition. Signal resonances are plotted as a function of signal frequency $\omega_s$ on an ordinary linear scale, with frequency increasing from left to right. The idler frequency scale is determined by that of the signal and the relationship $\omega_p = \omega_s + \omega_i$. In the display of idler resonances, therefore, frequency increases from right to left. A signal–idler pair that has both resonances centered on a vertical line are in coincidence, satisfying $\omega_p = \omega_s + \omega_i$. In general there will be some frequency mismatch $\Delta\omega$ for each mode pair. The frequency mismatch is the frequency shift that is required in order for either signal or idler resonance to produce coincidence. The detail on the left-hand side shows the frequency mismatch $\Delta\omega$ for a mode pair and its components $\Delta\omega_s$ and $\Delta\omega_i$, which are the respective frequency displacements from the centers of the signal and the idler cavity resonances to the frequencies most favorable for parametric oscillation. Dispersion is exaggerated in this schematic representation. There are typically hundreds of cavity axial modes between the cluster frequencies for which $\Delta\omega = 0$.

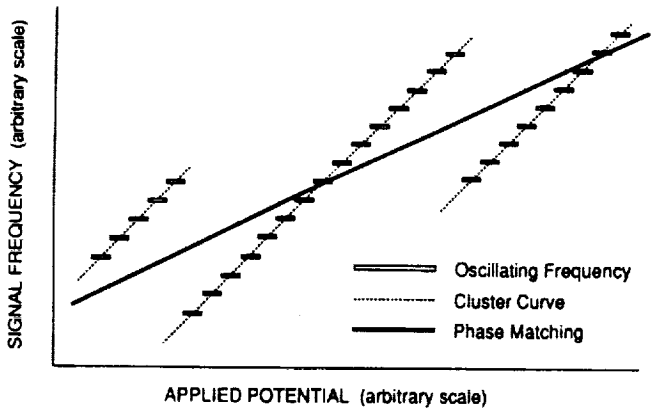


Fig. 4. Schematic representation of a detailed portion of an idealized tuning curve for a DRO. Oscillation progresses along cluster curves in discontinuous frequency changes, called axial mode hops, as a tuning variable is changed. A larger discontinuous frequency change, a cluster jump, occurs when better phase matching exists on an adjacent cluster curve.

Simultaneous resonance of signal–idler mode pairs occurs as a tuning parameter is continuously adjusted. In general, however, coincidence is not perfect, and oscillation of a particular mode pair depends on the degree of frequency matching and phase matching. The frequency mismatch $\Delta\omega$ of a signal–idler mode pair can be defined as the shift in frequency that is required of either the signal or the idler in order to bring the two resonances into coincidence to satisfy Eq. (1). It is convenient to express the frequency mismatch as the sum of two components:

$$\Delta\omega = \Delta\omega_s + \Delta\omega_i . \tag{3}$$

Here $\Delta\omega_s$ is the frequency shift from the peak of the signal resonance to the signal frequency that is most favorable for oscillation for that mode pair. Correspondingly, $\Delta\omega_i$ is the frequency shift from the peak of the idler resonance to the idler frequency that is most favorable for oscillation, as illustrated in Fig. 3. The signal component is measured on the signal frequency scale, and the idler component is measured on the idler frequency scale. The directions of these scales are opposite. One increases from left to right, and the other is reversed, increasing from right to left. Therefore $\Delta\omega_s$ and $\Delta\omega_i$ appear in opposite directions in Fig. 3, even though they have the same sign. The frequency displacements of the signal and idler from their respective resonance peaks are discussed in detail in Subsection 2.C. It is useful to consider the dependence of the OPO threshold on frequency mismatch and phase mismatch first.

### B. DRO Threshold with Imperfect Signal-Idler Frequency Coincidence

Even an extremely small frequency mismatch can have significant effects on frequency selection and threshold of the DRO, particularly when cavity finesse is high. The threshold relationship obtained here is the same as that derived in the quantum-mechanical analysis by Graham and Haken[9] and is similar to but more detailed than the threshold equation given by Giordmaine and Miller.[2] The result given here is in terms of classical electromagnetic theory and is more easily applied to the tuning analysis that follows. This threshold relationship is limited to cavities with moderate-to-infinitesimal losses. The effect of phase and frequency mismatch on the thresholds of DRO's with arbitrary cavity losses was discussed by Falk.[12] Falk's results are used to estimate the conditions under which the threshold equation used here is appropriate.

The threshold for oscillation is obtained by setting the parametric gain equal to the cavity losses. The electric fields of the pump, the signal, and the idler waves are expressed in terms of complex amplitude and exponentials:

$$E_j(z,t) = \tfrac{1}{2}[E_j(z)\exp\, i(k_j z - \omega_j t) + \text{c.c.}],$$

where the subscript $j$ indicates signal, idler, or pump, $k$ is the wave vector magnitude, $\omega$ is the angular frequency, $z$ is the coordinate in the direction of propagation, and $t$ is time. The couped equations that describe parametric amplification of monochromatic plane waves traveling in the $z$ direction are[7]

$$\frac{dE_s}{dz} = i\kappa_s E_p E_i^* \exp(i\Delta k z), \tag{4a}$$

$$\frac{dE_i}{dz} = i\kappa_i E_p E_s^* \exp(i\Delta k z), \tag{4b}$$

and

$$\frac{dE_p}{dz} = i\kappa_p E_s E_i \exp(-i\Delta k z), \tag{4c}$$

where mks units are used and $\kappa_s = \omega_s d_{\text{eff}}/(n_s c)$, $\kappa_i = \omega_i d_{\text{eff}}/(n_i c)$, and $\kappa_p = \omega_p d_{\text{eff}}/(n_p c)$, with $n_s$, $n_i$, and $n_p$ the respective refractive indices for the signal, the idler, and the pump, $c$ the velocity of light, and $d_{\text{eff}}$ the effective nonlinear-optical coefficient. The solution used here is derived under the assumptions that at threshold pump depletion is insignificant and that the respective changes in signal and pump amplitudes, $\Delta E_s$ and $\Delta E_i$, are small compared with the amplitudes. Hence $E_s$ and $E_i$ are treated as constants in calculating the changes, that is,

$$\Delta E_s = i\kappa_s E_p E_i^* l \,\text{sinc}(\Delta k l/2) \tag{5a}$$

and

$$\Delta E_i = i\kappa_i E_p E_s^* l \,\text{sinc}(\Delta k l/2). \tag{5b}$$

The length of the nonlinear crystal is again given by $l$, and the sinc function is defined by $\text{sinc}\, x = (\sin x)/x$.

For the low-loss DRO's considered here, Eqs. (5) are adequate for modeling the parametric gain. Other solutions to Eqs. (4) include general monochromatic plane-wave solutions[13] that permit both pump depletion and arbitrary changes in $E_s$ and $E_i$ and somewhat more restrictive solutions that involve no pump depletion but have arbitrarily large changes in $E_s$ and $E_i$.[5,7] A solution of the latter type was used[12] for threshold analysis of DRO's with arbitrary strength of resonance.

The parametric gain must compensate for both a decrease in amplitude and for the phase change that is due to propagation in the cavity. The phasor diagram shown in Fig. 5 helps to illustrate this discussion. After a round-trip cavity transit the signal electric-field amplitude is reduced by a factor $(1 - a_s)$, and the phase is shifted by an

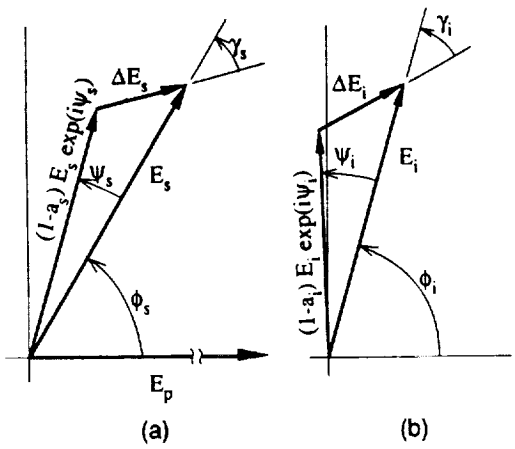


Fig. 5. Phasor diagrams schematically show amplitude losses $a_s$ and $a_i$ and phase shifts $\psi_s$ and $\psi_i$ after one round-trip cavity transit for the signal and the idler, respectively. At threshold the increments of electric-field amplitude added by optical parametric amplification, $\Delta E_s$ and $\Delta E_i$, must restore the original fields.

angle $\psi_s$. Similarly, the idler amplitude is reduced by $(1 - a_i)$, and the phase is shifted by $\psi_i$. At threshold this change is balanced by the increments of the electric field $\Delta E_s$ and $\Delta E_i$, added by the parametric interaction:

$$(1 - a_s)\exp(i\psi_s)E_s + \Delta E_s = E_s \tag{6a}$$

and

$$(1 - a_i)\exp(i\psi_i)E_i + \Delta E_i = E_i\,. \tag{6b}$$

Choosing time so that the pump amplitude is real, $E_p = |E_p|$, expressing the signal and idler amplitudes as $E_s = |E_s|\exp(i\phi_s)$ and $E_i = |E_i|\exp(i\phi_i)$, and applying the conditions that $a_s$, $a_i$, $\psi_s$, and $\psi_i$ are all small, we can write Eqs. (6) as

$$\Delta E_s = |E_s|(a_s^2 + \psi_s^2)^{1/2}\exp(i\phi_s - i\gamma_s) \tag{7a}$$

and

$$\Delta E_i = |E_i|(a_i^2 + \psi_i^2)^{1/2}\exp(i\phi_i - i\gamma_i)\,, \tag{7b}$$

where $\gamma_s = \tan^{-1}(\psi_s/a_s)$ and $\gamma_i = \tan^{-1}(\psi_i/a_i)$.

Substituting Eqs. (7) into Eqs. (5) results in two equations for the complex arguments and two equations for the magnitudes. The relationships for the complex arguments,

$$\phi_s + \phi_i = \gamma_s + \pi/2 \tag{8a}$$

and

$$\phi_s + \phi_i = \gamma_i + \pi/2 \tag{8b}$$

immediately yield $\gamma_s = \gamma_i$ for the stationary solution, or

$$\frac{\psi_s}{a_s} = \frac{\psi_i}{a_i}\,. \tag{9}$$

Note that Eqs. (8) are consistent with the result that the sum of the signal and idler phases is constant when referenced to the phase of the pump for stable single-mode-pair operation.[10]

The sum of the unpumped-cavity-round-trip phase shifts,

$$\psi = \psi_s + \psi_i\,, \tag{10a}$$

is useful for the purpose of comparison with the results of Ref. 12 and for conversion to frequency mismatch. When Eqs. (9) and (10a) are combined, the individual phase shifts can be expressed in terms of the sum by

$$\psi_s = \frac{a_s}{a_s + a_i}\psi \tag{10b}$$

and

$$\psi_i = \frac{a_i}{a_s + a_i}\psi\,. \tag{10c}$$

The threshold equation is obtained by taking the product of the two equations for the magnitudes that are obtained when Eqs. (7) are substituted into Eqs. (5), with the result that

$$[(a_s^2 + \psi_s^2)(a_i^2 + \psi_i^2)]^{1/2} = \kappa_s\kappa_i E_p^2 l^2\,\mathrm{sinc}^2(\Delta k l/2)$$
$$= \Gamma^2 l^2\,\mathrm{sinc}^2(\Delta k l/2)\,. \tag{11}$$

The quantity $\Gamma^2$ is the parametric gain for perfect phase matching, and it is proportional to the pump intensity.[7] With Eqs. (10b) and (10c), the threshold relationship given by Eq. (11) can be written in the form

$$\Gamma^2 l^2 = \frac{a_s a_i}{\mathrm{sinc}^2(\Delta k l/2)}\left[1 + \frac{\psi^2}{(a_s + a_i)^2}\right]. \tag{12}$$

Figure 6 shows the DRO threshold parameter $\Gamma^2 l^2$ as a function of the phase-shift sum $\psi$ as given by Eq. (12) for two sets of cavity losses $a_s = a_i = 0.0087$ and $a_s = a_i = 0.0033$, corresponding to finesse values $\mathcal{F} = 360$ and $\mathcal{F} = 960$ of the DRO's used in the experimental measurements. The shape of the threshold curve does not change significantly, but the minimum value is translated toward zero as the losses decrease. The width of the threshold

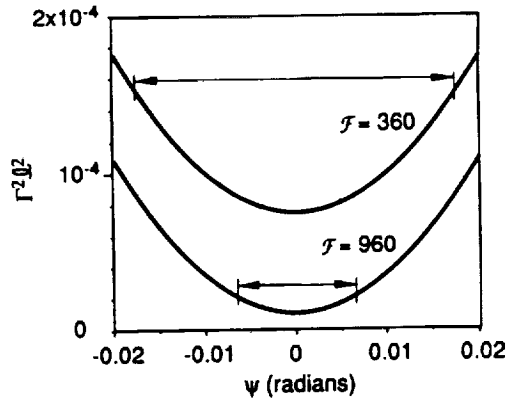


Fig. 6. Comparison of thresholds for DRO's with differing cavity finesses. Thresholds are calculated as a function of the sum of the cavity-round-trip phase shifts $\psi$ with Eq. (12) for two DRO's with cavity finesse $\mathcal{F}_s = \mathcal{F}_i = 360$ and $\mathcal{F}_s = \mathcal{F}_i = 960$. The shape of the curve does not change, but the width, defined as the region over which threshold is less than twice its minimum value, decreases for higher finesse.

curves, defined as the region over which threshold is less than twice the minimum value, therefore decreases as cavity losses decrease.

In the application of Eq. (12) thresholds are expressed in terms of cavity finesse because it is easier to measure the ratio of resonance width to spacing than it is to measure losses directly. A comparison of the above analysis with that of a parallel plate interferometer[14] or of optical cavities in general[15] shows that the amplitude loss coefficients $a_s$ and $a_i$ are related to the cavity finesse at signal and idler frequencies $\mathcal{F}_s$ and $\mathcal{F}_i$, respectively, by

$$\mathcal{F}_s \approx \pi/a_s, \qquad \mathcal{F}_i \approx \pi/a_i. \tag{13a,b}$$

It is also more convenient to use frequency mismatch than phase shift. The components of the frequency mismatch are related to the phase shifts by

$$\Delta\omega_s = \frac{\delta\omega_s\psi_s}{2\pi}, \qquad \Delta\omega_i = \frac{\delta\omega_i\psi_i}{2\pi}. \tag{14a,b}$$

When Eqs. (3), (10) and (12)-(14) are combined, the threshold equation becomes

$$\Gamma^2 l^2 = \frac{\pi^2}{\mathcal{F}_i\mathcal{F}_s \operatorname{sinc}^2(\Delta k l/2)}\left[1 + \left(\frac{2\Delta\omega\mathcal{F}_i\mathcal{F}_s}{\mathcal{F}_i\delta\omega_s + \mathcal{F}_s\delta\omega_i}\right)^2\right]. \tag{15}$$

The threshold relationship given by Eqs. (12) or (15) agrees with other threshold expressions under appropriate conditions. This result was obtained with a first-order plane-wave approximation for parametric gain. In the case of perfect phase matching, $\Delta k = 0$, and no frequency mismatch, $\Delta\omega = 0$, these equations reduce to $\Gamma^2 l^2 = a_s a_i$, which is the result obtained directly for this case.[7] Focusing and coupling to cavity modes[16] must be considered for quantitative threshold calculations. The plane-wave derivation of threshold is adequate for the analysis of tuning when it is necessary to know only the relative dependence of threshold on $\Delta k$ and $\Delta\omega$.

There is also agreement with the central result of Falk's analysis[12] in the limit of high cavity finesse, that is, $a_s \ll 1$ and $a_i \ll 1$. Rewritten in the notation used here, Falk's Eq. (9) becomes

$$\frac{\Gamma^2 l^2}{2} = \frac{B\sin\left[2\tan^{-1}\left(\dfrac{\sin\psi}{C+\cos\psi}\right) - \psi\right]}{\sin\left[\tan^{-1}\left(\dfrac{\sin\psi}{C+\cos\psi}\right)\right]\operatorname{sinc}^2\left(\dfrac{\Delta k l}{2}\right)} - \frac{1}{\operatorname{sinc}^2\left(\dfrac{\Delta k l}{2}\right)}, \tag{16}$$

where, defining $R_s = 1 - a_s$ and $R_i = 1 - a_i$,

$$B = \frac{R_i(1 - R_s^2)}{R_i^2 - R_s^2}, \qquad C = \frac{R_s}{R_i}\frac{1 - R_i^2}{1 - R_s^2}.$$

Equation (16) is a more accurate approximation of the DRO threshold applicable for arbitrary cavity loss. However, it is unwieldy and must be evaluated as a limit when $\psi = 0$ or when $a_s = a_i$. Evaluation of Eq. (12) yields threshold values that differ from those obtained from Eq. (16) by approximately the fraction $(a_s a_i)^{1/2}$. There is a fortuitous partial compensation for this disparity in the approximation for finesse given in Eqs. (13). For $\mathcal{F}_s = \mathcal{F}_i = 5$, the difference between Eqs. (15) and (16) is less than 13% at the frequency mismatch for which threshold is twice its minimum value, and the difference decreases with decreasing frequency mismatch. For $\mathcal{F}_s = \mathcal{F}_i = 10$, the difference is 4% at twice minimum threshold, and the agreement again improves as minimum threshold is approached.

Equations (12) or (15) could be used directly to determine the mode pair with the lowest threshold for oscillation. It is more convenient, however, to restrict the possible mode pairs on which oscillation may take place to a small number, based on frequency mismatch and wavevector mismatch considerations. This is done in Subsection 2.C, where it is shown that there are three mode pairs in the phase-matching bandwidth for which the frequency mismatch is a minimum. Which of these three mode pairs has the lowest threshold depends on the respective values of $\Delta k$, $\Delta\omega$, and the cavity finesse.

### C. Frequency Selection in the DRO

The selection of signal and idler frequencies in a cw DRO operating on a single mode pair is determined by two conditions: the conservation of energy stated in Eq. (1) and the minimum threshold for oscillation. An approximation for the threshold condition was given in Eq. (15). The conservation-of-energy condition becomes implicit in the analysis of the condition of minimum threshold. In this analysis it is convenient to follow the approach used by Boyd and Ashkin[3] and to define the signal and the idler axial mode numbers

$$m_s = 2ln_s/\lambda_s = ln_s\omega_s/(\pi c) \tag{17a}$$

and

$$m_i = 2ln_i/\lambda_i = ln_i\omega_i/(\pi c), \tag{17b}$$

which are continuous variables that take on integer values at cavity resonances. The free-space wavelengths of the signal and the idler are given by $\lambda_s$ and $\lambda_i$, respectively, and $2ln_s$ and $2ln_i$ are the respective optical lengths for a round-trip cavity transit. The free spectral ranges or mode spacings of the signal–idler resonances, $\delta\omega_s$ and $\delta\omega_i$, respectively, are the frequency changes that change the mode numbers $m_s$ and $m_i$ by one; that is,[4]

$$\frac{\partial m_s}{\partial\omega_s} = \frac{l}{\pi c}\left(n_s + \omega_s\frac{\partial n_s}{\partial\omega_s}\right) = \delta\omega_s^{-1} \tag{18a}$$

and

$$\frac{\partial m_i}{\partial\omega_i} = \frac{l}{\pi c}\left(n_i + \omega_i\frac{\partial n_i}{\partial\omega_i}\right) = \delta\omega_i^{-1}. \tag{18b}$$

The sum of the mode numbers

$$m = m_s + m_i, \tag{19}$$

which is also a continuous variable, is useful for the description of cluster effects. A signal frequency and an idler frequency that satisfy Eq. (1) and for which $m$ is an integer comprise a cluster frequency pair. In general, cavity resonances are not located precisely at the cluster frequencies. Only the sum $m_s + m_i$ must be an integer at the cluster frequencies; the individual mode numbers in general dif-

fer from integers by amounts equal in magnitude but opposite in sign. The cavity resonance pairs that most closely satisfy the conservation-of-energy condition and therefore that are most favorable for oscillation are also the resonances for which $m$ is most nearly an integer. Equivalently, oscillation frequencies of a DRO are displaced from a frequency pair at which $m$ is an integer by no more than one half of the respective axial mode spacings, whereas there are typically hundreds of modes between adjacent signal or idler cluster frequencies at which $m$ is an integer.

Two further quantities that are useful for the description of the mode hops and cluster jumps of DRO tuning, $\Delta m$ and $\Delta m_s$, are obtained by subtracting the integer nearest the mode number from the mode number:

$$\Delta m = m - \text{ROUND}(m) \tag{20a}$$

and

$$\Delta m_s = m_s - \text{ROUND}(m_s). \tag{20b}$$

These quantities are used in the calculation of oscillation frequencies and tuning-variable tolerances.

At optimum operating conditions, the quantities $\Delta k$, $\Delta m$, and $\Delta m_s$ will all be zero, indicating perfect phase matching and simultaneous cavity resonances at the desired signal and idler frequencies. Adjustment of three independent parameters is necessary in order to reach this condition. The discussion presented here is given in general terms with quantities $\Delta k$, $m$, *and* $m_s$ and in specific terms of the tuning or control parameters that are used in the experimental observations. The experimental observations use temperature $T$ and applied potential $V$ as adjustable parameters to control the output signal frequency $\omega_s$. Pump frequency $\omega_p$ is used as the required third adjustable parameter for the calculations. Simple Taylor's expansions for $\Delta k$, $m$, *and* $m_s$ were found to be adequate for modeling the observed frequency tuning:

$$\Delta k = \left(\frac{\partial \Delta k}{\partial \omega_s}\right)_{\omega_p} (\omega_s - \omega_{s,0}) + \frac{1}{2}\left(\frac{\partial^2 \Delta k}{\partial \omega_s^2}\right)_{\omega_p} (\omega_s - \omega_{s,0})^2 + \left(\frac{\partial \Delta k}{\partial \omega_p}\right)_{\omega_s} (\omega_p - \omega_{p,0}) + \frac{\partial \Delta k}{\partial T}(T - T_0) + \frac{\partial \Delta k}{\partial V} V + \Delta k_0, \tag{21}$$

$$m = \left(\frac{\partial m}{\partial \omega_s}\right)_{\omega_p} (\omega_s - \omega_{s,0}) + \frac{1}{2}\left(\frac{\partial^2 m}{\partial \omega_s^2}\right)_{\omega_p} (\omega_s - \omega_{s,0})^2 + \left(\frac{\partial m}{\partial \omega_p}\right)_{\omega_s} (\omega_p - \omega_{p,0}) + \frac{\partial m}{\partial t}(T - T_0) + \frac{\partial m}{\partial V} V + m_0, \tag{22}$$

and

$$m_s = \frac{\partial m_s}{\partial \omega_s}(\omega_s - \omega_{s,0}) + \frac{1}{2}\frac{\partial^2 m_s}{\partial \omega_s^2}(\omega_s - \omega_{s,0})^2 + \frac{\partial m_s}{\partial T}(T - T_0) + \frac{\partial m_s}{\partial V} V + m_{s,0}. \tag{23}$$

A second-order derivative is used for signal frequency because the first-order derivatives $(\partial \Delta k/\partial \omega_s)_{\omega_p}$ and $(\partial \Delta m/\partial \omega_s)_{\omega_p}$ become zero at degeneracy, and dispersion of $\partial m_s/\partial \omega_s$ is essential to the analysis.

The notation of a partial derivative in parentheses with a parameter subscript to the right-hand parenthesis indicates that the parameter of the subscript is held constant for the differentiation. The conservation-of-energy condition is introduced through this device. Consider a function that is dependent on the signal, the idler, and the pump frequencies $f = f(\omega_s, \omega_i, \omega_p)$, and require that the conservation-of-energy condition $\omega_s + \omega_i = \omega_p$ hold. Differentiation with respect to $\omega_s$, with $\omega_p$ held constant, requires that as $\omega_s$ is increased $\omega_i$ must decrease, or

$$\left(\frac{\partial f}{\partial \omega_s}\right)_{\omega_p} = \frac{\partial f}{\partial \omega_s} - \frac{\partial f}{\partial \omega_i},$$

and, similarly,

$$\left(\frac{\partial f}{\partial \omega_p}\right)_{\omega_s} = \frac{\partial f}{\partial \omega_p} + \frac{\partial f}{\partial \omega_i}.$$

The derivatives used in Eqs. (21)–(23) are expanded in Table 1. The differentiation is straightforward and can be verified by inspection of Eqs. (2), (17), and (19).

**Table 1. Derivatives Used to Calculate Tuning of a Monolithic DRO**

$$\frac{\partial^2 m_s}{\partial \omega_s^2} = \frac{l}{\pi c}\left(2\frac{\partial n_s}{\partial \omega_s} + \omega_s \frac{\partial n_s^2}{\partial \omega_s^2}\right)$$

$$\frac{\partial m_s}{\partial T} = \frac{l\omega_s}{\pi c}\frac{\partial n_s}{\partial T} + \frac{\omega_s n_s}{\pi c}\frac{\partial l}{\partial T}$$

$$\frac{\partial m_s}{\partial V} = \frac{\omega_s}{\pi c}\left(n_s \frac{\partial l}{\partial V} + l\frac{\partial n_s}{\partial V}\right)$$

$$\left(\frac{\partial m}{\partial \omega_s}\right)_{\omega_p} = \frac{l}{\pi c}\left(n_s - n_i + \omega_s \frac{\partial n_s}{\partial \omega_s} - \omega_i \frac{\partial n_i}{\partial \omega_i}\right)$$

$$\left(\frac{\partial^2 m}{\partial \omega_s^2}\right)_{\omega_p} = \frac{l}{\pi c}\left[2\left(\frac{\partial n_s}{\partial \omega_s} + \frac{\partial n_i}{\partial \omega_i}\right) + \omega_s \frac{\partial^2 n_s}{\partial \omega_s^2} + \omega_i \frac{\partial^2 n_i}{\partial \omega_i^2}\right]$$

$$\left(\frac{\partial m}{\partial \omega_p}\right)_{\omega_s} = \frac{l}{\pi c}\left(n_i + \omega_i \frac{\partial n_i}{\partial \omega_i}\right)$$

$$\frac{\partial m}{\partial T} = \frac{l}{\pi c}\left(\omega_s \frac{\partial n_s}{\partial T} + \omega_i \frac{\partial n_i}{\partial T}\right) + \frac{1}{\pi c}(\omega_s n_s + \omega_i n_i)\frac{\partial l}{\partial T}$$

$$\frac{\partial m}{\partial V} = \frac{n_s \omega_s + n_i \omega_i}{\pi c}\frac{\partial l}{\partial V} + \frac{l}{\pi c}\left(\omega_s \frac{\partial n_s}{\partial V} + \omega_i \frac{\partial n_i}{\partial V}\right)$$

$$\left(\frac{\partial \Delta k}{\partial \omega_s}\right)_{\omega_p} = \left(n_i - n_s + \omega_i \frac{\partial n_i}{\partial \omega_i} - \omega_s \frac{\partial n_s}{\partial \omega_s}\right)\Big/ c = -\frac{\pi}{l}\left(\frac{\partial m}{\partial \omega_s}\right)_{\omega_p}$$

$$\left(\frac{\partial^2 \Delta k}{\partial \omega_s^2}\right)_{\omega_p} = -\frac{\pi}{l}\left(\frac{\partial^2 m}{\partial \omega_s^2}\right)_{\omega_p}$$

$$\left(\frac{\partial \Delta k}{\partial \omega_p}\right)_{\omega_s} = \left(n_p - n_i + \omega_p \frac{\partial n_p}{\partial \omega_p} - \omega_i \frac{\partial \omega_i}{\partial \omega_i}\right)$$

$$\frac{\partial \Delta k}{\partial T} = \frac{\omega_p}{c}\frac{\partial n_p}{\partial T} - \frac{\omega_s}{c}\frac{\partial n_s}{\partial T} - \frac{\omega_i}{c}\frac{\partial n_i}{\partial T}$$

$$\frac{\partial \Delta k}{\partial V} = \frac{\omega_p}{c}\frac{\partial n_p}{\partial V} - \frac{\omega_s}{c}\frac{\partial n_s}{\partial V} - \frac{\omega_i}{c}\frac{\partial n_i}{\partial V}$$

### 1. *Phase-Matching Curve and Cluster Curves*

A number of equations considered below are identical except for the exchange of the tuning variables. An economy of notation is possible through the use of a general tuning parameter $\zeta$, which is $T$, $V$, or $\omega_p$ in the specific example or, more generally, is any single parameter used to tune a DRO. A phase-matching curve gives the signal frequency for which $\Delta k = 0$ as a function of the tuning parameter $\zeta$ and as used here is denoted by $\omega_{s,\mathrm{PM}}(\zeta)$. This curve is obtained from Eq. (21) or from a similar equation by setting the other adjustable parameters to fixed values and setting $\Delta k = 0$. The cluster curves $\omega_{s,\mathrm{Cl}}(\zeta)$ give the signal cluster frequencies as a function of the tuning parameter $\zeta$. The cluster curves can be obtained from Eq. (22) or from a similar equation by setting $m$ to integer values and again setting the other adjustable parameters to fixed values. For type-I phase matching, the phase-matching curve is a parabolalike curve, as shown in Fig. 2, and the cluster curves are a family of parabolalike curves. The oscillating frequencies are closest to the cluster curves near the points where the cluster curves intersect the phase-matching curve.

The signal frequency separation of adjacent clusters $\Omega_s$ can be obtained from the second-order approximation

$$\Delta m(\text{cluster}) = \pm 1 = \left(\frac{\partial m}{\partial \omega_s}\right)_{\omega_p} \Omega_{S\pm} + \frac{1}{2}\left(\frac{\partial^2 m}{\partial \omega_s^2}\right)_{\omega_p} \Omega_{S\pm}{}^2. \quad (24)$$

Away from degeneracy the first-order term dominates, and Eq. (24) is approximated by

$$\Omega_{S\pm} \approx \pm\left(\frac{\partial m}{\partial \omega_s}\right)_{\omega_p}^{-1} = \pm\frac{\delta\omega_i \delta\omega_s}{\delta\omega_i - \delta\omega_s}, \quad (25)$$

in agreement with Ref. 4. Phase-matching limitations result in a gain bandwidth with half-maximum values at the frequencies for which $\Delta k \approx \pm 0.886\pi/l \approx \pm\pi/l$ and a corresponding signal frequency full width at half-maximum of

$$\Delta\omega_s(\text{Gain FWHM}) \approx \left|\frac{2\pi}{l}\left(\frac{\partial \Delta k}{\partial \omega_s}\right)_{\omega_p}^{-1}\right|. \quad (26)$$

In the specific case of the monolithic DRO, for which derivatives are given in Table 1, $\pi/l(\partial m/\partial\omega_s)_{\omega_p} = -(\partial\Delta k/\partial\omega_s)_{\omega_p}$ and $\Delta\omega_s(\text{Gain FWHM}) \approx 2\Omega_S$. Since the frequency separation of the clusters is approximately one half of the parametric gain bandwidth, there are two or three clusters within the gain bandwidth. This is true for any DRO in which the nonlinear crystal is the only dispersive component and the crystal is traversed twice in each round-trip cavity transit but has parametric gain in only one direction.

### 2. *Oscillation Frequencies*

The oscillation frequencies are determined by phase matching, the center frequencies of the signal and the idler cavity resonances, the frequency mismatch of the resonances, the finesse values of the resonances, and the axial mode spacings. To model experimental observations, we calculate the frequencies of the parametric oscillation by the following procedure. First the signal frequency for phase matching $\omega_{s,\mathrm{PM}}$ is found for specified tuning parameters with the condition $\Delta k = 0$. Next the signal cluster frequency $\omega_{s,\mathrm{Cl}}$ that is closest to $\omega_{s,\mathrm{PM}}$ is found with the condition $\Delta m = 0$. If the DRO cavity has only moderate or low finesse and if the precise oscillating frequency and mode hops are not of concern, these two steps are all that are required. The extra resolution of frequency tuning can be obtained using the value of $\Delta m_s$ at the cluster frequency $\omega_{s,\mathrm{Cl}}$. This value is called $\Delta m_{s,\mathrm{Cl}}$ to indicate that it is calculated at the cluster frequency $\omega_{s,\mathrm{Cl}}$ for the specified tuning conditions.

The procedure for determining the fine details of tuning is illustrated in Fig. 7. The signal cluster frequency $\omega_{s,\mathrm{Cl}}$, obtained by the steps described above, is a reference point from which to start. The center of the nearest signal resonance is displaced from $\omega_{s,\mathrm{Cl}}$ by frequency $-\Delta m_{s,\mathrm{Cl}}\delta\omega_s$, where $\delta\omega_s$ is the signal axial mode frequency separation. The center of the nearest idler resonance is displaced by $-\Delta m_{i,\mathrm{Cl}}\delta\omega_i$ from the complementary idler cluster frequency $\omega_{i,\mathrm{Cl}} = \omega_p - \omega_{s,\mathrm{Cl}}$, where $\delta\omega_i$ is the idler mode frequency separation and $\omega_p$ is the pump frequency. Since $\omega_{s,\mathrm{Cl}}$ is a cluster frequency with $\Delta m = 0$, then $\Delta m_{i,\mathrm{Cl}} = -\Delta m_{s,\mathrm{Cl}}$, which permits the frequency mismatch of the signal–idler mode pair to be expressed as

$$\Delta\omega = \Delta m_{s,\mathrm{Cl}}(\delta\omega_s - \delta\omega_i). \quad (27)$$

Recall that the frequency mismatch is the shift in frequency of either the signal or the idler resonance that is necessary in order to bring the resonance pair into coincidence to satisfy the conservation-of-energy condition.

The displacement of the signal oscillation frequency $\omega_{s,\mathrm{Osc}}$ from the center of the signal cavity resonance is $\Delta\omega_s$, and the displacement of the idler oscillation frequency $\omega_{i,\mathrm{Osc}}$ from the center of the idler cavity resonance is $\Delta\omega_i$. From the above definitions and conditions imposed on round-trip cavity phase shifts for a stationary solution given in Eqs. (3), (10), (13), and (14), it follows that

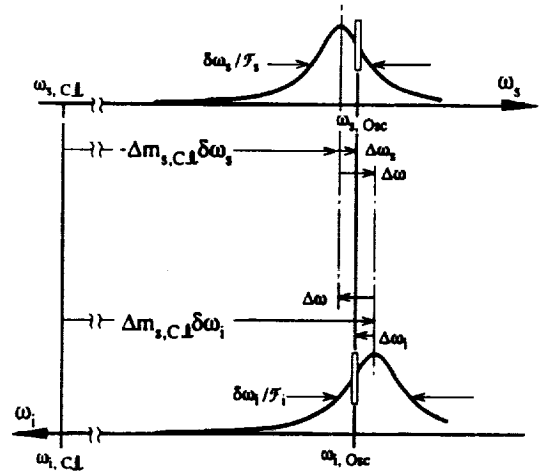


Fig. 7. Signal-idler resonance diagram similar to Fig. 3, expanded in detail to show the relationships between quantities. The signal and the idler cavity resonances on which oscillation occurs are displaced from the respective cluster frequencies $\omega_{s,\mathrm{Cl}}$ and $\omega_{i,\mathrm{Cl}}$ for the general case of nonzero frequency mismatch. The DRO oscillating frequencies $\omega_{s,\mathrm{Osc}}$ and $\omega_{i,\mathrm{Osc}}$ divide the frequency mismatch $\Delta w$ into the components $\Delta\omega_s$ and $\Delta\omega_i$.

$$\Delta\omega_s = \Delta\omega\delta\omega_s\mathcal{F}_i/(\delta\omega_s\mathcal{F}_i + \delta\omega_i\mathcal{F}_s) \tag{28a}$$

and

$$\Delta\omega_i = \Delta\omega\delta\omega_i\mathcal{F}_s/(\delta\omega_s\mathcal{F}_i + \delta\omega_i\mathcal{F}_s). \tag{28b}$$

Finally, the signal oscillation frequency is given by the sum of the cluster frequency plus the frequency separation of the signal cavity resonance from the cluster frequency plus the frequency shift from the center of the signal cavity resonance, that is,

$$\begin{aligned}\omega_{s,\mathrm{Osc}} &= \omega_{s,\mathrm{Cl}} - \Delta m_{s,\mathrm{Cl}}\delta\omega_s + \Delta\omega_s \\ &= \omega_{s,\mathrm{Cl}} - \Delta m_{s,\mathrm{Cl}}\frac{\delta\omega_s\delta\omega_i(\mathcal{F}_s + \mathcal{F}_i)}{\delta\omega_s\mathcal{F}_i + \delta\omega_i\mathcal{F}_s}.\end{aligned} \tag{29}$$

Equations (27) and (28a) are used to obtain the second step of Eq. (29).

The rate of frequency change associated with a general tuning parameter $\zeta$ could be obtained by direct differentiation of Eq. (29) or more simply by considering the tuning rates of the cavity resonances. The tuning rate for the frequency of the signal mode is $-\delta\omega_s(\partial m_s/\partial\zeta)$ and that for the frequency of the idler is $-\delta\omega_i(\partial m_i/\partial\zeta)$. The tuning rates of the cavity resonances are combined to yield the rate of change of the frequency mismatch,

$$\frac{\partial\Delta\omega}{\partial\zeta} = \delta\omega_s\frac{\partial m_s}{\partial\zeta} + \delta\omega_i\frac{\partial m_i}{\partial\zeta} = (\delta\omega_s - \delta\omega_i)\frac{\partial m_s}{\partial\zeta} + \delta\omega_i\frac{\partial m}{\partial\zeta}.$$

The tuning rate of the signal oscillation frequency is the sum of the tuning rate of the signal resonance plus the fraction $\delta\omega_s\mathcal{F}_i/(\delta\omega_s\mathcal{F}_i + \delta\omega_i\mathcal{F}_s)$ of $\partial\Delta\omega/\partial\zeta$, that is,

$$\frac{\partial\omega_{s,\mathrm{Osc}}}{\partial\zeta} = \frac{\delta\omega_s\delta\omega_i}{\delta\omega_s\mathcal{F}_i + \delta\omega_i\mathcal{F}_s}\left(\mathcal{F}_i\frac{\partial m}{\partial\zeta} - (\mathcal{F}_s + \mathcal{F}_i)\frac{\partial m_s}{\partial\zeta}\right). \tag{30}$$

This tuning is limited to a small range by mode hops or increased cavity losses as the oscillation is pulled off the peaks of the cavity resonances. On a broader scale, tuning progresses along a cluster curve in a series of mode hops. If finesse is high, it is possible that the oscillation jumps back and forth between adjacent cluster curves and also hops from one mode pair to the next along each of the cluster curves. The analysis of cluster jumps requires that the mode-hop structures on the two or three cluster curves that are closest to phase matching be compared in order to determine which cluster curve provides conditions most favorable for oscillation.

The tuning rates in the regions between mode hops and cluster jumps, which are described by Eq. (30), are strongly dependent of the relative values of finesse of the signal and the idler cavity resonances. Some caution, however, is required in the use of Eq. (30). For example, the calculation of $\partial\omega_{s,\mathrm{Osc}}/\partial V$ and $\partial\omega_{s,\mathrm{Osc}}/\partial T$ for DRO's with nearly equal signal and idler finesse involves the small difference of two quantities. In such situations it is important that the terms on the right-hand side of Eq. (30) be evaluated accurately for the specified operating conditions.

*3. Tuning Limits and Mode Hops*

Mode hops are periodic along the cluster curves, occurring every time $m_{s,\mathrm{Cl}}$ changes by one. Recall that $m_{s,\mathrm{Cl}}$ is the value of $m_s$ on the cluster curve for which $\Delta m = 0$. The change of the tuning parameter $\Delta\zeta_{\mathrm{Hop\ spacing}}$ that corresponds to a mode hop is a quantity that is easily measured experimentally. Since a mode hop corresponds to a change of one in $m_{s,\mathrm{Cl}}$, it follows that the tuning parameter change that corresponds to the mode-hop spacing is

$$\Delta\zeta_{\mathrm{Hop\ spacing}} = \left|\left(\frac{\partial m_{s,\mathrm{Cl}}}{\partial\zeta}\right)^{-1}\right|. \tag{31}$$

In the evaluation of $\partial m_{s,\mathrm{Cl}}/\partial\zeta$ it is helpful to use the derivative

$$\begin{aligned}\frac{\partial\omega_{s,\mathrm{Cl}}}{\partial\zeta} &= -\frac{\partial m}{\partial\zeta}\left(\frac{\partial m}{\partial\omega_s}\right)^{-1}_{\omega_p} \\ &= -\frac{\delta\omega_s\delta\omega_i}{\delta\omega_i - \delta\omega_s}\frac{\partial m}{\partial\zeta}.\end{aligned} \tag{32}$$

The first step simply states that the cluster frequency $\omega_{s,\mathrm{Cl}}$ must change with the tuning parameter $\zeta$ in such a way that $m$ does not change, and the second step is accomplished by using Eqs. (18) and (19). It is possible to expand the derivative $\partial m_{s,\mathrm{Cl}}/\partial\zeta$ by first using the chain rule of differentiation and then Eqs. (18) and (32) to obtain

$$\frac{\partial m_{s,\mathrm{Cl}}}{\partial\zeta} = \frac{\partial m_s}{\partial\zeta} + \frac{\partial m_s}{\partial\omega_s}\frac{\partial\omega_{s,\mathrm{Cl}}}{\partial\zeta} = \frac{\partial m_s}{\partial\zeta} - \frac{\delta\omega_i}{\delta\omega_i - \delta\omega_s}\frac{\partial m}{\partial\zeta}. \tag{33}$$

Another useful parameter is the maximum frequency shift from the cluster curve that can be achieved without a mode hop ($\omega_{s,\mathrm{Hop}} - \omega_{s,\mathrm{Cl}}$). This maximum is obtained directly when the extreme values of $\Delta m_{s,\mathrm{Cl}} = \pm 1/2$ are inserted into Eq. (29), yielding

$$\omega_{s,\mathrm{Hop}} - \omega_{s,\mathrm{Cl}} = \pm\frac{1}{2}\frac{\delta\omega_i\delta\omega_s(\mathcal{F}_i + \mathcal{F}_s)}{\delta\omega_i\mathcal{F}_s + \delta\omega_s\mathcal{F}_i}. \tag{34}$$

Cavity finesse can also limit the single-parameter tuning range. It follows from Eq. (15) that threshold is double its minimum value when the frequency mismatch $\Delta\omega$ reaches the value

$$\Delta\omega = \pm\frac{\mathcal{F}_i\delta\omega_s + \mathcal{F}_s\delta\omega_i}{2\mathcal{F}_i\mathcal{F}_s}.$$

The corresponding value of $\Delta m_{s,\mathrm{Cl}}$ is obtained from Eq. (27). On substitution into Eq. (29) the maximum displacement of signal oscillation frequency from the cluster frequency allowed by cavity finesse is found to be

$$\omega_{s,\mathrm{Fin}} - \omega_{s,\mathrm{Cl}} = \pm\frac{\mathcal{F}_s + \mathcal{F}_i}{2\mathcal{F}_s\mathcal{F}_i}\frac{\delta\omega_s\delta\omega_i}{\delta\omega_i - \delta\omega_s}. \tag{35}$$

If finesse is large the frequency displacement allowed by Eq. (35) becomes significantly smaller than the frequency displacement required for a mode hop described by Eq. (34). In this case parametric oscillation on the cluster curve closest to phase matching ceases in a region near the mode hop. It is then possible for the parametric oscillation frequencies to jump to an adjacent cluster curve that is still within the phase-matching gain bandwidth if a favorable coincidence of signal and idler resonances exists on that cluster curve.

Plotting the mode-hop frequency limits $\omega_{s,\mathrm{Hop}}$ and the finesse frequency limits $\omega_{s,\mathrm{Fin}}$ in addition to the cluster curve provides additional information concerning the fine detail of tuning. On a broader scale, it is informative to display curves defining the phase-matching gain bandwidth along with the phase-matching curve. It may also be useful to display more than one cluster curve near the phase-matching curve.

An attempt was made to keep the results of this section general. For application to the specific case of a monolithic DRO tuned by temperature, applied potential, and pump frequency, the appropriate variables and derivatives from Table 1 are directly substituted for the terms involving the general tuning parameter $\zeta$. Evaluation of the derivatives for the case of monolithic DRO's made from $MgO:LiNbO_3$ with propagation in the $x$ direction and with an electric field applied in the $y$ direction is discussed in Appendix A. Temperature-dependent dispersion, thermal expansion, the electro-optic effect, and the piezoelectric effect of the nonlinear-optical material are used in the evaluation. Results of this evaluation for experimental conditions described in Section 3 are given in Table 2.

## 3. EXPERIMENTAL OBSERVATIONS AND MODELING

### A. Experimental Conditions

Two monolithic DRO's, which were described previously,[17,18] were used in the experimental observations. One DRO had lower finesse and had to be pulse-pumped in order to achieve the higher threshold power needed for parametric oscillation. The higher-finesse DRO operated above threshold with the available continuous pumping. The pump source was a diode-laser-pumped nonplanar ring oscillator,[19,20] constructed of neodymium-doped yttrium aluminum garnet (Nd:YAG) with the 1064-nm laser output converted to 532 nm by externally resonant second-harmonic generation.[21] Approximately 30 mW of cw pump radiation was generated. The laser operated in a single longitudinal and a single transverse mode. For cw operation of the laser fundamental frequency stability was typically 10 kHz over short periods of time.[22,23] This value was doubled at the second harmonic. Higher peak power at similar average power was obtained by driving the laser into relaxation oscillations by 10% amplitude modulation of the diode-laser output at 320 kHz. Good frequency stability and high optical quality of the pump radiation, such as that achieved with the diode-laser-pumped solid-state laser, are important for obtaining stable DRO performance.

Both monolithic DRO's were operated with a ring-resonator configuration. They were constructed from 5% magnesium-oxide-doped lithium niobate ($MgO:LiNbO_3$).[24,25] Each of these monolithic resonators was 12.5-mm long with the crystal $x$ axis in the long direction. A ring path in these resonators was formed by reflections from two multilayer dielectric coated surfaces with 10-mm radii of curvature and a totally internally reflecting surface. The centers of curvature of the spherical surfaces were on a line parallel to and 180 μm inside the flat totally internally reflecting surface. A drawing of the monolithic DRO's is shown in Fig. 8. The 532-nm pump beam was mode matched for collinear propagation on the segment of the ring path parallel to the crystal $x$ axis. The pump beam with extraordinary polarization did not follow the closed path of the signal and the idler waves with ordinary polarization because of birefleection.

Metal coatings for electric-field tuning were applied to the crystal surfaces perpendicular to the $y$ axis. The thickness of the crystals between the electrodes was

**Table 2. Derivatives used to Model Tuning of $MgO:LiNbO_3$ Monolithic DRO's[a]**

| | |
|---|---|
| $\frac{\partial m_s}{\partial \omega_s}$ | $= 3.05 \times 10^{-11}\ (\mathrm{rad/sec})^{-1}$ |
| $\left(\frac{\partial m}{\partial \omega_s}\right)_{\omega_p}$ | $= 0$ |
| $\left(\frac{\partial \Delta k}{\partial \omega_s}\right)_{\omega_p}$ | $= 0$ |
| $\frac{\partial^2 m_s}{\partial \omega_s^2}$ | $= 1.10 \times 10^{-27}\ (\mathrm{rad/sec})^{-2}$ |
| $\left(\frac{\partial^2 m}{\partial \omega_s^2}\right)_{\omega_p}$ | $= 2.20 \times 10^{-27}\ (\mathrm{rad/sec})^{-2}$ |
| $\left(\frac{\partial^2 \Delta k}{\partial \omega_s^2}\right)_{\omega_p}$ | $= -5.53 \times 10^{-35}\ \frac{\mathrm{rad/m}}{(\mathrm{rad/sec})^2}$ |
| $\frac{\partial m_s}{\partial \omega_p}$ | $= 0$ |
| $\left(\frac{\partial m}{\partial \omega_p}\right)_{\omega_s}$ | $= 3.05 \times 10^{-11}\ (\mathrm{rad/sec})^{-1}$ |
| $\left(\frac{\partial \Delta k}{\partial \omega_p}\right)_{\omega_s}$ | $= 5.44 \times 10^{-10}\ \frac{\mathrm{rad/m}}{\mathrm{rad/sec}}$ |
| $\frac{\partial m_s}{\partial T}$ | $= 1.02°\mathrm{C}^{-1}$ |
| $\frac{\partial m}{\partial T}$ | $= 2.03°\mathrm{C}^{-1}$ |
| $\frac{\partial \Delta k}{\partial T}$ | $= 749\ \frac{\mathrm{rad/m}}{°\mathrm{C}}$ |
| $\frac{\partial m_s}{\partial V}$ | $= \frac{-1.81 \times 10^{-6}\ \mathrm{m/V}}{t}$ |
| $\frac{\partial m}{\partial V}$ | $= \frac{-3.63 \times 10^{-6}\ \mathrm{m/V}}{t}$ |
| $\frac{\partial \Delta k}{\partial V}$ | $= \frac{3.61 \times 10^{-4}}{t}\ \frac{\mathrm{rad/m}}{\mathrm{V/m}}$ |

[a] The parameter $t$ is the effective thickness of the crystal in meters; $l = 0.0125$ m, $\omega_{s,0} = 3.54070 \times 10^{15}$ rad/sec, $\omega_{i,0} = 1.77035 \times 10^{15}$ rad/sec, $T_0 = 107.04°\mathrm{C}$, $V_0 = 0$.

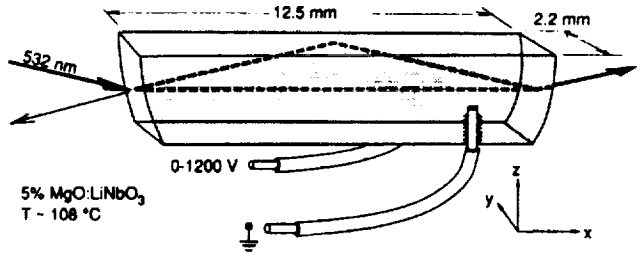


Fig. 8. DRO geometry used for experimental observations.

2.2 mm. The finesse of both DRO's at 1.064 $\mu$m was measured with the Nd:YAG laser output directly, without second-harmonic generation. Electric-field tuning was used to scan the resonators through a free spectral range, and transmission through the resonators gave a measure of resonance width relative to the mode spacing. One DRO had a finesse of 360, and the other had finesse of 960. The lower-finesse device had an experimentally observed threshold for cw parametric oscillation of 35 mW, and the higher-finesse DRO had a threshold of 12 mW. The pump source could produce approximately 30 mW of cw radiation at 532 nm. The higher-threshold OPO was pumped by 532-nm second harmonic, which consisted of 400-nsec pulses with 230-mW peak power at a 320-kHz repetition rate.

The output of the DRO's was tuned by temperature and electric field. Noncritical phase matching in MgO:$LiNbO_3$ was achieved for degeneracy at 107°C, and as temperature was increased the signal and the idler wavelengths separated from the 1.064-$\mu$m degeneracy point. For the tuning studies the potential applied to the crystal was repetitively ramped at fixed temperature. Output wavelength measurements were repeated at incrementally changed temperatures. An $f/10$, 1-m grating monochromator with a 600-line/mm grating was used for wavelength measurement. The DRO output directed into the monochromator consisted of a series of pulses; these pulses resulted either from the pulse pumping or from the mode hops produced by the ramped voltage with continuous pumping. The radiation transmitted by the monochromator usually consisted of a few pulses in a narrow spectral band that could be correlated with the potential applied to the DRO electrodes. A schematic representation of the experimental setup is shown in Fig. 9.

## B. Cluster Tuning

The tuning of the high-finesse DRO involved spectral jumps back and forth between cluster curves as well as mode hops along the cluster curves. This behavior is illustrated in Fig. 10, where DRO output is displayed for a small voltage range at a constant temperature. In this figure output is resolved on three separate cluster curves. The monochromator slits were opened to provide a 5-nm

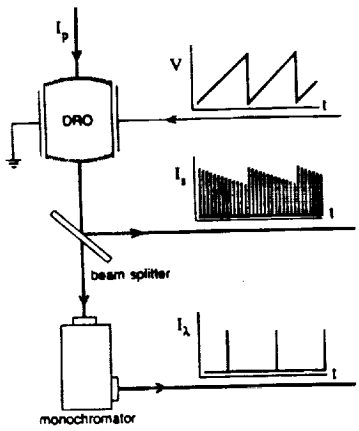


Fig. 9. Schematic representation of the setup used for DRO tuning measurements.

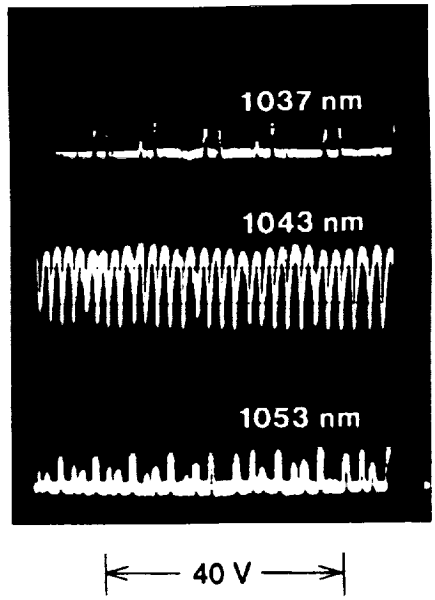


Fig. 10. Oscillograms of cw-pumped DRO output, showing simultaneous output on three cluster curves. The signal displayed is that produced by a photodiode placed after a monochromator with slits adjusted for a 5-nm bandpass. Each of the oscillograms corresponds to the same portion of the ramped voltage applied to the DRO. The change in applied potential is indicated. The oscillograms differ only in the wavelength setting of the monochromator, indicated for the individual traces. The output on the central cluster dominates and is so strong that the oscilloscope trace does not return to the baseline.

transmission width, one sufficient to resolve the individual clusters while transmitting a number of mode hops. The central cluster curve with signal wavelength near 1043 nm dominated. Two other cluster curves fit within the phase-matching gain bandwidth, and output on these curves was observed near 1053 and 1037 nm. Competition with the central cluster curve, which depletes the pump wave, is evident in the two cluster curves to either side.

Three adjustable parameters were used to fit Eqs. (21) and (22) to the observations. A temperature-offset correction is used to fit the calculated phase-matching curve. There are inaccuracies in both the absolute measurement of temperature and in the temperature dependence of the dispersion relationships that make this necessary. The temperature adjustment was accomplished by shifting the data a fraction of 1°C but could have equally well been done by changing the parameter $\Delta k_0$ in Eq. (21). Another fitting parameter is required because the optical lengths of the DRO's are not precisely known. This fit is accomplished by changing the value of $m_0$ in Eq. (22) and has the effect of adjusting the placement of the cluster curves. The thickness of the DRO crystals is also used as a fitting parameter. The electrodes do not completely cover the surfaces, and fringing effects are not considered. Instead, it is assumed that there is a uniform electric field in the $y$ direction given by $E_y = V/t$, where $V$ is the applied potential and $t$ is an effective thickness. Adjusting the thickness has the effect of changing the slopes of the cluster curves and voltage-tuned phase-matching curve. It is interesting to note that the piezoelectric effect, in addition to the electro-optic effect, is needed to model the ob-

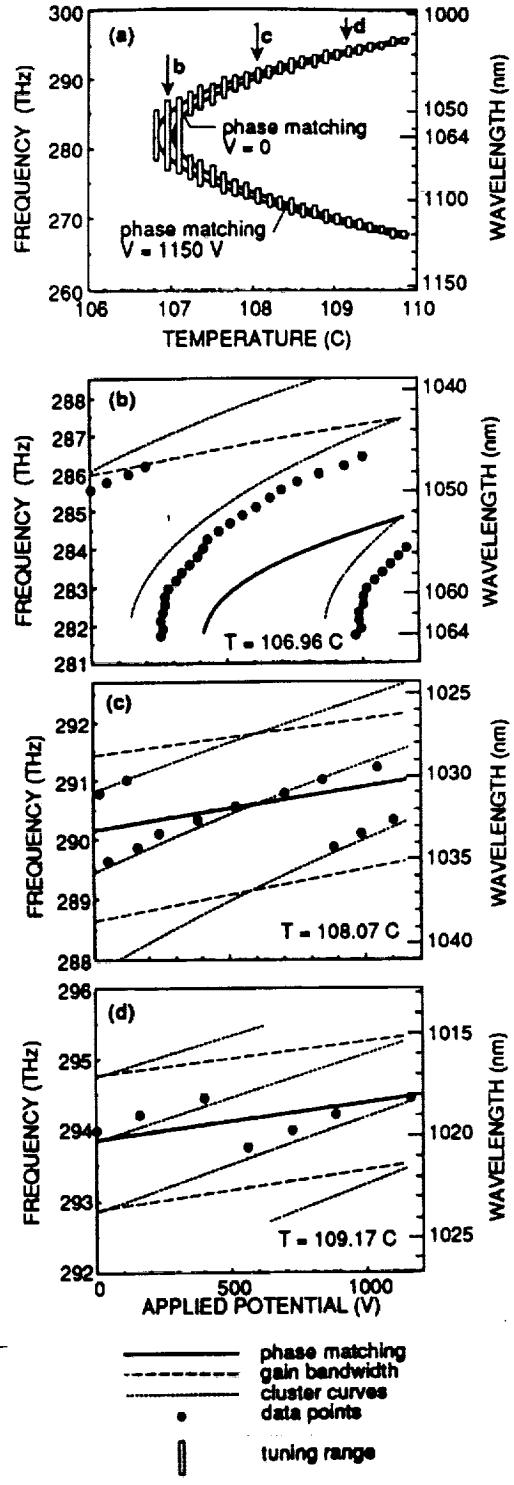


Fig. 11. Observed and calculated tuning for the pulsed-pumped DRO with finesse of 360. The open vertical bars in (a) show the extent of tuning observed as applied potential was ramped from 0 to 1150 V at a constant temperature. The solid curves behind the vertical bars are calculated phase-matching curves for the extreme voltages. Voltage tuning for three temperatures is shown in (b)–(d), where the bold central curves are the calculated phase-matching curves, and the dashed curves indicate the limits of the phase-matching bandwidth. The dotted curves are calculated cluster curves, and the filled circles are observed operating points of the DRO. This DRO, which has only moderate finesse, exhibits few jumps between cluster curves as the voltage is ramped. The data are measurements of the applied potential for a limited sampling of output frequencies and do not represent individual mode hops.

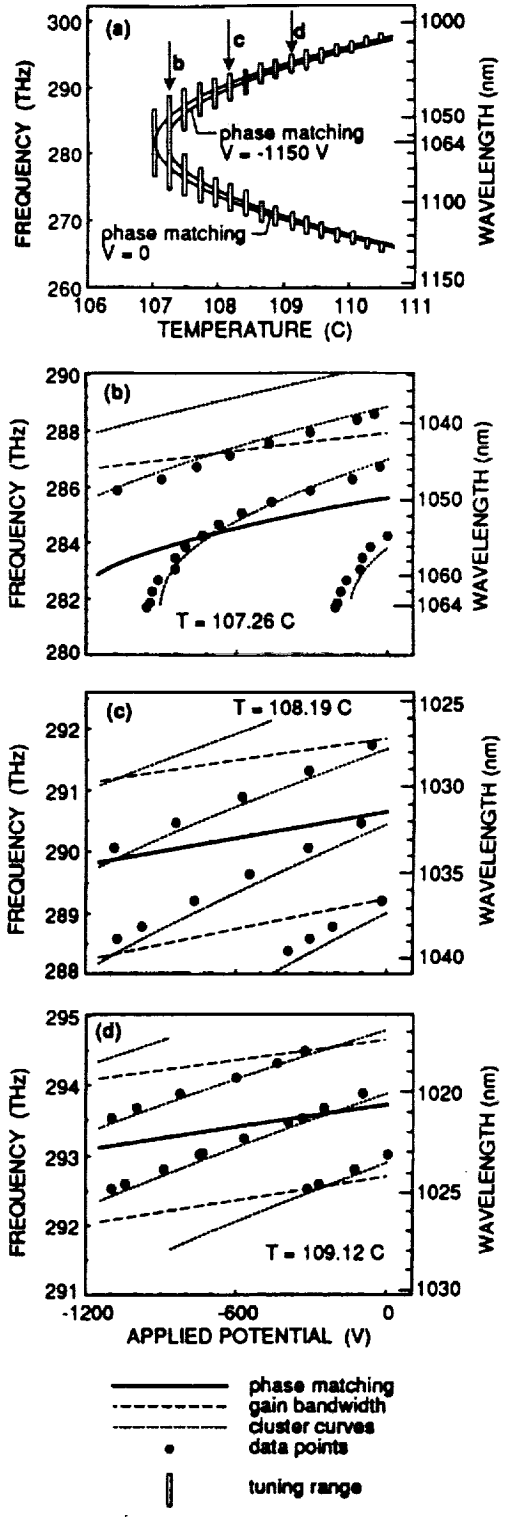


Fig. 12. Observed and calculated tuning for the cw-pumped DRO with finesse of 960. As in Fig. 11, the open bars in (a) indicate the range of tuning as voltage was ramped, in this case between −1150 V and 0, and the solid curves behind the vertical bars are the calculated phase-matching curves for the two extreme voltages. Voltage tuning is shown for three temperatures in (b)–(d). This DRO, which has higher finesse, exhibits a number of frequency jumps between three cluster curves as voltage is tuned.

served tuning. When only the electro-optic effect is used, the calculated voltage-tuned cluster curves are parallel to the voltage-tuned phase-matching curve. A fourth fitting parameter not used here is the constant $m_{s,0}$ in Eq. (23). Adjustment of $m_{s,0}$ would allow for different phase shifts at the mirror surfaces for the signal and the idler and the possibility of different cavity lengths.[3] Adjustment of $m_{i,0}$ would change the calculated position of the mode hops.

The observed and fitted tuning curves for the DRO's are shown in Figs. 11 and 12. The theory is most easily expressed in terms of frequency. Frequency therefore is used as the primary ordinate scale in these graphs, and wavelength is included as a secondary scale for reference. The temperature-tuned phase-matching curves are shown in Figs. 11(a) and 12(a). At each temperature setting a range of output wavelengths is obtained by voltage tuning. In most cases the observed tuning ranges cover the space between and extend slightly beyond the calculated temperature-dependent tuning curves for the extreme voltages. Voltage was ramped from 0 to 1150 V, and when the crystal was reversed from 0 to −1150 V. Figures 11(b)–11(d) and 12(b)–12(d) show the voltage tuning at selected fixed temperatures. The data are the voltages at which output was observed at selected frequencies. Calculated phase-matching curves, gain-bandwidth curves, and cluster curves are shown for comparison. In some instances the data are located in lines parallel to the calculated cluster curves but not on the cluster curves. This most likely is caused by inaccuracy in temperature measurement, and coincidence could be obtained by choosing a different temperature calibration for each setting. In practice DRO tuning may provide an accurate measurement of its temperature. The DRO sensitivity to temperature will become more apparent below when the details of tuning are discussed.

Figures 11 and 12 appear to be similar in a cursory examination; however, one aspect of tuning's dependence on finesse is illustrated. The lower-finesse DRO, with the tuning shown in Fig. 11, usually oscillates on the single cluster curve nearest the phase-matching curve. Sometimes the oscillation jumps back and forth between two cluster curves when they are nearly equally distant from phase matching. The output of the higher-finesse DRO with the tuning shown in Fig. 12 jumps between two or three cluster curves. This is in agreement with theoretical predictions that show the tuning limit imposed on the $\mathcal{F} = 960$ DRO by the resonance widths; that is, the finesse limit of tuning is reached before the mode-hop limit of tuning for most conditions encountered.

The cluster curves are also dependent on temperature. The data displayed in Fig. 12 are interpreted to show temperature tuning at constant voltage in Fig. 13. Here the data points are either interpolated from measurements of cluster tuning with voltages both higher and lower than the selected voltage or extrapolated from measurements of the cluster curves that nearly reach the selected voltage. The calculated phase matching, gain bandwidth, and cluster curves are again in reasonable agreement with observation.

### C. Axial Mode-Hop tuning

There is good agreement between observation and the calculated voltage change required to produce a mode hop. Observations similar to those illustrated in Fig. 10 were performed under various conditions. The results are shown in Fig. 14, in which $\Delta V_{\text{Hop spacing}}$ is displayed as a function of detuning from degeneracy. The calculated line is obtained from Eqs. (31) and (33). The tuning parameter is voltage, and it is necessary to substitute $V$ for $\zeta$ in the equations and further to substitute the appropriate values from Table 2, and to evaluate the derivative $(\partial m/\partial \omega_s)_{\omega_p}$ as a function of signal frequency. The approximations given in Section 4 by relations (37) and (38) also work well in the evaluation of Eq. (31).

Calculations of axial-mode-hop tuning along cluster curves were performed for conditions that would approximate those used to produce Fig. 10. The same fitting parameters were used as in Figs. 12 and 13. An operating temperature and center voltage were chosen to give three cluster curves centered on phase matching at the

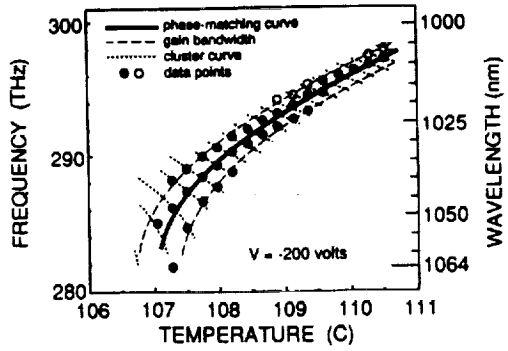


Fig. 13. Observed and calculated tuning for the cw-pumped DRO as a function of temperature. The same tuning data that was used in Fig. 12 is used here. A fixed voltage of −200 V was chosen. For the cases in which oscillation on a cluster curve was observed at voltages both higher and lower than this voltage, frequencies were obtained by interpolation and are represented by filled circles. For the cases in which cluster tuning came near but did not reach this voltage, frequencies were obtained by extrapolation and are represented by open circles. The dotted curves are portions of the calculated temperature-dependent cluster curves. The calculated phase-matching curve is the central bold curve, and the dashed curves show the approximate gain-bandwidth limits.

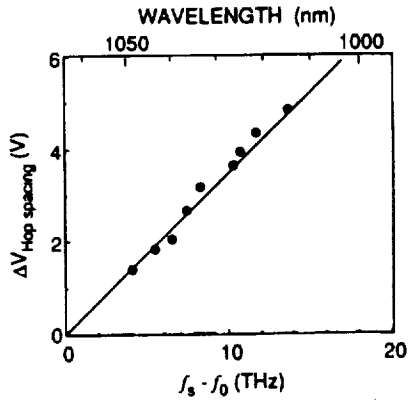


Fig. 14. Mode-hop spacing in an applied potential as a function of detuning from degeneracy. The dots are data points and the solid line is calculated from theory.

observed operating frequencies. This was done by manipulation and solution of Eqs. (21) and (22). Calculated phase-matching, gain-bandwidth, and cluster curves in this region are shown in Fig. 15(a). Calculated tuning along the three cluster curves with the detail of mode hops is shown in Figs. 15(b)–15(d). These tuning curves were obtained by using Eq. (22) to calculate the cluster signal frequency $\omega_{s,Cl}$, Eq. (23) to calculate the signal mode number $m_{s,Cl}$ at the cluster frequency, and Eq. (29) to calculate the signal frequency of the oscillation. The mode-hop frequency limits given by Eq. (34) and the finesse frequency limits given by Eq. (35) are also shown.

When the oscillating signal frequency differs from the cluster signal frequency by more than the mode-hop limit, it is advantageous for the oscillation to shift to another signal-idler resonance pair. When the oscillating frequency excursion from the cluster frequency reaches the finesse limit, the threshold for parametric oscillation is double the value it had when the oscillation frequencies coincided with the cluster frequencies, and the threshold increases for greater excursions of the oscillation frequency from the cluster frequency. Figure 15 illustrates how cluster jumps can be interspersed with the mode hops of a single cluster curve. For the calculation presented in Fig. 15, the finesse limit of tuning is reached before the mode-hop limit is reached on the central cluster curve shown in Fig. 15(c). Parametric oscillation on the central cluster curve usually dominates, because phase matching is best there. When the finesse limit of the frequency excursion from the cluster curve is reached, however, the parametric oscillation on the central cluster curve decays, and it is possible to have oscillation build up on an adjacent cluster curve before oscillation can build up on the next mode pair of the central cluster curve. Notice that the mode-hop spacing that is measured by the change in the tuning variable is different for the three adjacent cluster curves of Fig. 15(b)–15(d). Also, the relative positions of the finesse and mode-hop limits change with detuning from degeneracy.

These comparisons show quantitative agreement between observations and the tuning theory of Section 2. The tuning theory describes the cluster tuning of the DRO as well as the effects of cavity finesse on the cluster structure in the occurrence of cluster jumps. Also, the theory is able to predict the observed spacing in the tuning variable of axial mode hops on a microscopic scale of tuning. This is done with temperature-dependent dispersion, thermal expansion, and electro-optical and piezoelectric effects. Only three fitting parameters are used: a temperature calibration, which entailed the translation of a temperature scale by a fraction of a degree Celsius, an adjustment of cavity length $l$ of less than one wavelength, and the use of a effective crystal thickness that compensated for the nonuniformity of the electric field inside the crystal. With this agreement it is reasonable to consider applying the theory to analysis of the DRO for optical frequency synthesis. Specifically, the analysis addresses conditions that are necessary to reproduce the coherence of a frequency-stable pump with a small degree of tunability at any frequency in the tuning range of the DRO.

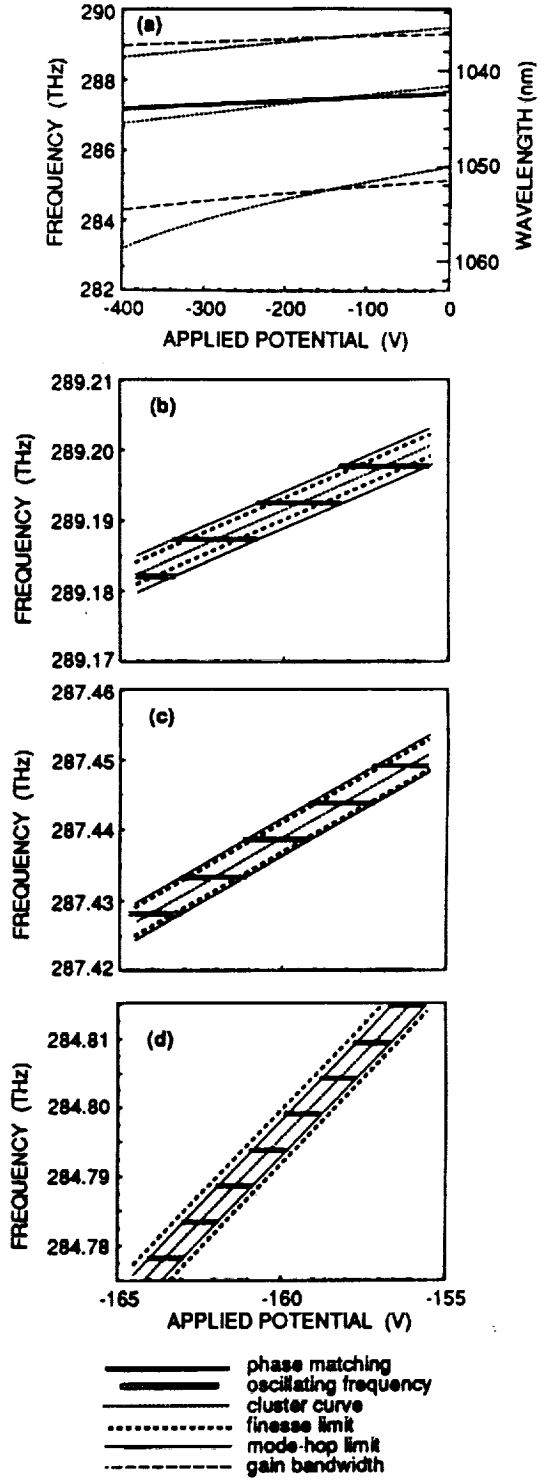


Fig. 15. Detailed display of calculated DRO tuning as a function of applied potential for conditions that would produce output similar to that shown in Fig. 10. All calculations are for a fixed temperature of 107.540°C. Detailed calculations of tuning for three cluster curves are shown in (b)–(d). Here the DRO output frequency is indicated by the open horizontal bars. A finesse of 960 is used.. The slope of the continuous portions of the detailed tuning curves (b)–(d) is dependent on the relative values of finesse at the signal and the idler frequencies, but in all cases the slope is much less than that of the cluster curves.

## 4. FREQUENCY SYNTHESIS AND TUNING-VARIABLE TOLERANCES

Parameter tolerances and continuous frequency tuning are topics that can be addressed with the theory presented above. Knowledge of tolerances is important for stable DRO operation and for tuning to oscillation at specific frequencies. Continuous frequency tuning is of interest in many applications. Fixed-frequency operation with resolution finer than a mode hop may be required, or perhaps truly continuous frequency coverage may be necessary. The DRO output frequencies lie within the widths of cavity resonances. The extent of continuous tuning depends on several factors, including frequency shifts of the cavity modes, the spectral range over which the conservation of energy condition can be satisfied while maintaining oscillation within a selected mode pair, and the spectral range over which higher net parametric gain is not available on another mode pair. Multiple-parameter tuning, in which two or more parameters are synchronously changed, is required for continuous tuning over the full free spectral range of the oscillator. Single-parameter tuning will provide frequency coverage over small regions that are separated by the discrete mode hops.

It is easiest to think of tolerances for situations in which only a single parameter is permitted to change. In practice there are advantages in dealing with parameter tolerances in pairs. For example, voltage and temperature adjustments could be used to maintain stable oscillation at a fixed frequency. It may not be possible to control temperature to the precision that is required if voltage is fixed, but the lack of adequate temperature control could be offset by voltage control. Feedback techniques could be used to adjust voltage in order to maintain stable oscillation on a signal–idler mode pair even in the presence of temperature fluctuations that by themselves would cause mode hops. The change in voltage required for stable operation could be used as an error signal that would in turn be used to return the temperature to the desired value.

Simultaneous adjustment of three parameters could also be used to tune the output frequency of the DRO. As an example, consider a pump frequency that is ramped in some specified way. The conditions required for stable operation on a single signal–idler mode pair could be provided by feedback control of the potential applied for electro-optic and piezoelectric tuning. The tolerance required for phase matching would be much less stringent than that required for stable operation on a single signal–idler mode pair; adequate phase matching could be maintained by temperature control, based on a functional relationship that is dependent on the pump frequency and voltage required for stable operation. With two-parameter tuning frequency matching could be maintained, but it would not be possible to maintain optimum phase matching.

### A. Tuning-Variable Tolerances

The parameter tolerances for stable operation are determined by the more restrictive of two conditions. Mode hops are avoided by operation within a range of adjustment over which higher gain does not develop on another signal–idler mode pair. The range of adjustment over which oscillation can be maintained on a mode pair may be limited to a smaller value by the resonance width or equivalently by the DRO finesse. These tolerances are closely related to the mode-hop spacing and spectral limits of tuning that were discussed above, and they can be obtained from detailed tuning curves such as those shown in Fig. 15(b)–15(d) for voltage tuning. Detailed tuning curves for temperature tuning and pump-frequency tuning are shown in Figs. 16 and 17, respectively.

The conditions for the calculations displayed in Figs. 16 and 17 are the same as those used to produce Fig. 15(c). These conditions are $\mathcal{F}_s = \mathcal{F}_i = 960$ for a MgO:$LiNbO_3$ DRO of length $l = 1.25$ cm, pumped at 564 THz (532 nm) with signal frequency near 287 THz (1043 nm). Fitting parameters used in these calculations, such as an effective thickness $t = 0.277$ cm and a length adjustment corresponding to a change in $m$ of 0.42, are the same as those required to fit the experimental data in Figs. 12 and 13. These characteristics are carried forward to other calculations for the purpose of providing a specific example for comparison.

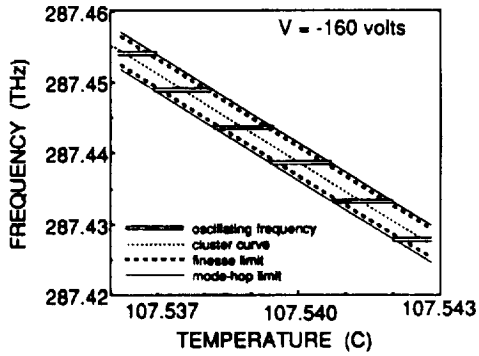


Fig. 16. Calculated detailed tuning as a function of temperature. For this calculation temperature is adjusted while other parameters are held constant at values that correspond to a point near the center of Fig. 15(c). Here, also, the slope of the continuous portions of the tuning curve are dependent on the relative values of signal and idler finesse, and this slope is small compared with the slope of the cluster curve.

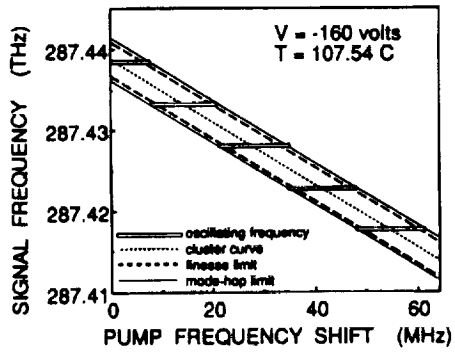


Fig. 17. Calculated detailed tuning as a function of pump frequency. For this calculation pump frequency is adjusted while other parameters are held constant at values that correspond to a point near the center of Fig. 15(c). For pump-frequency tuning with equal signal and idler cavity finesse, the slope of the continuous portions of the tuning curve is −0.5. Because of the scale necessary to display the much greater slope of the cluster curve, the continuous portions of the tuning curve appear to be horizontal.

The detailed tuning curves of Figs. 15–17 are similar in many respects. The mode-hop and finesse limits of frequency displacement from the cluster curve are independent of the tuning parameter. In each of the figures the slope of the continuous portion of tuning between mode hops is much smaller than the slope of the cluster curve. The slopes of the continuous portions of tuning are dependent on the relative finesse of the signal and the idler resonances. The case of equal finesse is shown in the calculated tuning curves. The illustrated curves show that voltage must be held within a tolerance of approximately 1 V, temperature within 0.0006°C, and pump frequency within 7 MHz for stable operation in this example.

Analytic approximations for the parameter tolerances for stable operation are not limited to a specific example. The range over which a parameter can be changed without causing a mode hop is obtained from the condition $\Delta m_{s,Cl} = \pm 1/2$. Recall that $m_{s,Cl}$ is the value $m_s$ for a point on the associated cluster curve, and the cluster curve is a line that gives the values of signal frequency $\omega_s$ and a tuning parameter $\zeta$ for which $\Delta m = 0$, with the other parameters held at fixed values. It follows that the tuning-parameter tolerance is

$$\Delta\zeta_{\text{Hop tolerance}} = \pm\frac{1}{2}\left(\frac{\partial m_{s,Cl}}{\partial\zeta}\right)^{-1}. \tag{36}$$

The derivative in the above equation can be evaluated with Eq. (33). An approximation of that equation for the case of type-I phase matching is given by

$$\frac{\partial m_{s,Cl}}{\partial\zeta} \approx -\frac{\delta\omega_0}{\delta\omega_i - \delta\omega_s}\frac{\partial m}{\partial\zeta}, \tag{37}$$

where $\delta\omega_0$ is the mode spacing at degeneracy ($\omega_s = \omega_i = \omega_0 = \omega_p/2$). The difference between the idler and the signal mode spacing can also be expanded about degeneracy by using Eqs. (18) to obtain

$$\delta\omega_i - \delta\omega_s \approx 2\delta\omega_0{}^2\frac{\partial^2 m_s}{\partial\omega_s^2}(\omega_s - \omega_0). \tag{38}$$

Equation (36) and relations (37) and (38) can be combined to give the desired approximation for the mode-hop parameter tolerance, namely,

$$\Delta\zeta_{\text{Hop tolerance}} \approx \pm\delta\omega_0\frac{\partial^2 m_s}{\partial\omega_s^2}(\omega_s - \omega_0)\Big/\frac{\partial m}{\partial\zeta}. \tag{39}$$

The adjustable parameter tolerance related to cavity finesse can be obtained from the cavity-round-trip phase-shift sum for which the pumping threshold is twice its minimum value. From Eqs. (12) and (13) this phase-shift sum is

$$\psi_{\text{Fin}} = \pm\pi\left(\frac{1}{\mathcal{F}_i} + \frac{1}{\mathcal{F}_s}\right). \tag{40}$$

Since $\psi = 2\pi\Delta m$, the parameter tolerance determined by cavity finesse is

$$\Delta\zeta_{\text{Fin tolerance}} \approx \pm\frac{\frac{1}{2}(1/\mathcal{F}_i + 1/\mathcal{F}_s)}{\partial m/\partial\zeta}. \tag{41}$$

**Table 3. Calculated Single-Parameter Continuous Tuning Rates and Parameter Tolerances for Stable Operation of the Finesse = 960 DRO Pumped at 563.6 THz with Signal Frequency 287.44 THz**

| Tuning Parameter $\zeta$ | $\frac{\partial f_{s,\text{Osc}}}{\partial\zeta}$ | $\Delta\zeta_{\text{Hop tolerance}}$ | $\Delta\zeta_{\text{Fin tolerance}}$ |
|---|---|---|---|
| $V$ (Voltage) | 72 kHz/V | ±0.98 V | ±0.80 V |
| $T$ (Temperature) | −124 MHz/°C | ±0.00064°C | ±0.00051°C |
| $f_p$ (Pump Frequency) | 0.499 Hz/Hz | ±6.7 MHz | ±5.4 MHz |

The parameter tolerance related to mode hops, given by relation (39), is zero at degeneracy and increases linearly with detuning from degeneracy. In practice, however, operation precisely at degeneracy was stable for tens of minutes with no adjustments to the DRO.[10] The parameter tolerance related to cavity finesse, given by relation (41), remains approximately constant independent of detuning from degeneracy as long as finesse remains constant. Calculated tuning-variable tolerances are given in Table 3 for the MgO:$LiNbO_3$ DRO for the conditions used to generate Figs. 15(c), 16, and 17.

## B. Single-Parameter Tuning

The cavity resonances associated with the signal wave and the idler wave can have significantly different finesse. The oscillating frequencies of the DRO will more closely align with the higher-finesse cavity resonance rather than the complementary resonance with lower finesse and greater width. If the frequencies of the cavity resonances change, the oscillation will follow the higher-finesse resonance more closely, to the extent possible without a mode hop or cluster jump. If the pump frequency changes, the frequency of the wave oscillating on the higher-finesse cavity resonance will remain more nearly constant than that of the wave oscillating on the lower-finesse resonance. In this sense the higher-finesse resonance pulls the frequencies of oscillation more strongly.

It has been noted by Smith[4] that the continuous tuning of a DRO is relatively insensitive to tuning-parameter changes that change the optical length of the DRO resonator, but the signal frequency and the idler frequency both display approximately one half of the change that occurs in pump frequency. Single parameter continuous tuning is described by Eq. (30), which can be rewritten with $m = m_s + m_i$ as

$$\frac{\partial\omega_{s,\text{Osc}}}{\partial\zeta} = \frac{\delta\omega_s\delta\omega_i}{\delta\omega_i\mathcal{F}_s + \delta\omega_s\mathcal{F}_i}\left(\mathcal{F}_i\frac{\partial m_s}{\partial\zeta} - \mathcal{F}_s\frac{\partial m_i}{\partial\zeta}\right).$$

In the mathematical development used here, $\omega_s$ and $\omega_p$ are used as independent variables, with $\omega_i$ determined by Eq. (1). Choosing pump frequency $\omega_p$ as the variable parameter $\zeta$ requires the substitutions

$$\frac{\partial m_i}{\partial\zeta} \to \left(\frac{\partial m_i}{\partial\omega_p}\right)_{\omega_s} = \frac{\partial m_i}{\partial\omega_i}$$

and

$$\frac{\partial m_s}{\partial \zeta} \rightarrow \left(\frac{\partial m_s}{\partial \omega_p}\right)_{\omega_s} = 0.$$

The signal and the idler mode spacings, $\delta\omega_s$ and $\delta\omega_i$, will differ by only a small amount, and if $\mathcal{F}_s$ and $\mathcal{F}_i$ are nearly equal, the tuning rate is $\partial\omega_{s,\mathrm{Osc}}/\partial\omega_p \approx 1/2$. More generally, for differing values of finesse, the tuning rate is in the range $0 < \partial\omega_{s,\mathrm{Osc}}/\partial\omega_p < 1$. Even though approximately half the pump frequency tuning will be reflected in signal tuning, only a relatively small spectral range will be covered before a mode hop is encountered. Calculated single-parameter tuning rates for the special case of $\mathcal{F}_s = \mathcal{F}_i$, corresponding to the DRO's described in Section 3, are given in Table 3. The partial derivatives needed in this calculation were evaluated for $\omega_{s,\mathrm{Osc}} = 287.44$ THz (1043 nm) and $T_0 = 107.51$°C instead of being taken from Table 2. As explained in subsection 2.C.2, this procedure is required for the evaluation of $\partial f_{s,\mathrm{Osc}}/\partial V$ and $\partial f_{s,\mathrm{Osc}}/\partial T$, which involve the small difference in two quantities, but has little effect on the other values in the table.

### C. Multiple-Parameter Tuning

It is possible to extend the continuous tuning range by synchronously adjusting two or three parameters. Adjusting two parameters simultaneously permits the conditions $\Delta m = 0$ and $\Delta m_s = 0$ to be maintained, but $\Delta k$ will change. Adjusting three parameters simultaneously permits tuned parametric oscillation while $\Delta m$, $\Delta m_s$, and $\Delta k$ all remain equal to zero for a specified mode pair, and tuning is limited only by the extent that the parameters can be changed.

Generalized tuning parameters with adjustable $\zeta_1$ and $\zeta_2$ and fixed $\zeta_3$ are used for the discussion of two-parameter tuning. For the specific case treated here, any permutation of voltage, temperature, and pump frequency can be used for these three parameters. The conditions $\Delta m = 0$ and $\Delta m_s = 0$ determine a relationship between $\zeta_1$ and $\zeta_2$, and use of this relationship permits $\omega_s$ and $\Delta k$ to be expressed as functions of $\zeta_1$. These relationships can be obtained by first differentiating Eqs. (21)–(23) with respect to $\zeta_1$, yielding

$$\frac{\mathrm{d}m}{\mathrm{d}\zeta_1} = 0 = \left(\frac{\partial m}{\partial \omega_s}\right)_{\omega_p} \frac{\mathrm{d}\omega_s}{\mathrm{d}\zeta_1} + \frac{\partial m}{\partial \zeta_1} + \frac{\partial m}{\partial \zeta_2}\frac{\mathrm{d}\zeta_2}{\mathrm{d}\zeta_1}, \tag{42a}$$

$$\frac{\mathrm{d}m_s}{\mathrm{d}\zeta_1} = 0 = \frac{\partial m_s}{\partial \omega_s}\frac{\mathrm{d}\omega_s}{\mathrm{d}\zeta_1} + \frac{\partial m_s}{\partial \zeta_1} + \frac{\partial m_s}{\partial \zeta_2}\frac{\mathrm{d}\zeta_2}{\mathrm{d}\zeta_1}, \tag{42b}$$

and

$$\frac{\mathrm{d}\Delta k}{\mathrm{d}\zeta_1} = \left(\frac{\partial \Delta k}{\partial \omega_s}\right)_{\omega_p} \frac{\mathrm{d}\omega_s}{\mathrm{d}\zeta_1} + \frac{\partial \Delta k}{\partial \zeta_1} + \frac{\partial \Delta k}{\partial \zeta_2}\frac{\mathrm{d}\zeta_2}{\mathrm{d}\zeta_1}. \tag{42c}$$

Only a small spectral region is being considered, and it is unnecessary to consider second partial derivatives with respect to signal frequency. The first partial derivatives, however, must be evaluated for the operating conditions that are being considered. A specific case for which this consideration is important is frequency tuning for voltage and temperature adjustment, which again involves a small difference of terms. Equations (42a) and (42b) are solved for $\mathrm{d}\omega_s/\mathrm{d}\zeta_1$ and $\mathrm{d}\zeta_2/\mathrm{d}\zeta_1$. These values are substituted into Eq. (42c) to yield a value for $\mathrm{d}\Delta k/\mathrm{d}\zeta_1$. Results are calculated for three sets of tuning parameters and are listed in Table 4. The conditions used for these calculations are the same as those used for Figs. 15–17 and Table 3; the partial derivatives in Eqs. (42) again were evaluated for $\omega_{s,\mathrm{Osc}} = 287.44$ THz (1043 nm) and $T_0 = 107.561$°C.

Two of the examples given in Table 4 are briefly noted. The voltage–temperature tuning mentioned earlier is of interest for operation at a fixed frequency. The rate of change of the output frequency with applied potential when the voltage and the temperature are changed simultaneously in order to maintain $\Delta m = 0$ and $\Delta m_s = 0$ is calculated to be −7.9 kHz/V. The magnitude of this tuning rate is about 10 times smaller than the single-parameter voltage tuning rate given in Table 3 and significantly smaller than the 3.5-MHz/V tuning rate of the cavity resonance. The reduced sensitivity is important in stable-frequency operation of the DRO. Simultaneous pump-frequency and voltage tuning is useful for continuous coverage of the spectral region between the mode hops of single-parameter tuning. Calculated tuning curves for this case are shown in Fig. 18. The same conditions used in Figs. 15–17 apply again to Fig. 18. Tuning is taken to the limits of $\Delta k = \pm\pi/l$ in the figure.

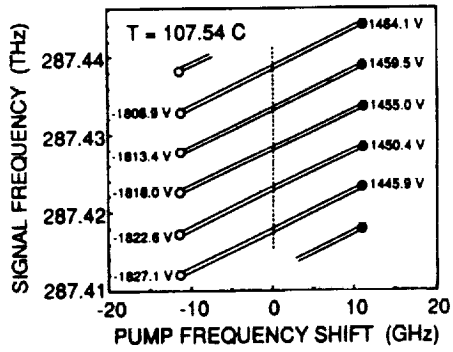


Fig. 18. Calculated tuning for varying the voltage and the pump frequency simultaneously so as to maintain $\Delta m = 0$ and $\Delta m_s = 0$. The dashed line is the cluster curve of Fig. 17. Tuning limits are taken at the point at which $\Delta k = \pm p/l$ in the 1.25-cm-long crystal.

**Table 4. Calculated Values for Two-Parameter Tuning of a Monolithic MgO:LiNbO$_3$ DRO at $f_s = 287.44$ THz or $\lambda_s = 1043$ nm**

| Adjustable Parameters | Fixed Parameter | $\frac{\mathrm{d}f_s}{\mathrm{d}\zeta_1}$ | $\frac{\mathrm{d}\zeta_2}{\mathrm{d}\zeta_1}$ | $\frac{\mathrm{d}\Delta k}{\mathrm{d}\zeta_1}$ |
|---|---|---|---|---|
| $\zeta_1 = f_p$, $\zeta_2 = V$ | $T = 107.54$°C | 0.510 | $1.47 \times 10^{-7}$ V/Hz | $2.26 \times 10^{-8}$ (rad/m)/Hz |
| $\zeta_1 = f_p$, $\zeta_2 = T$ | $V = -160$ V | 0.511 | $(-9.4 \times 10^{-11})$°C/Hz | $-6.7 \times 10^{-8}$ (rad/m)/Hz |
| $\zeta_1 = V$, $\zeta_2 = T$ | $f_p = 563.6$ THz | −7.9 kHz/V | $(6.4 \times 10^{-4})$°C/V | 0.613 (rad/m)/V |

Two methods of three-parameter tuning are presented. First a method is described for achieving oscillation at a specified frequency while satisfying the conditions $\Delta k = 0$, $\Delta m = 0$, and $\Delta m_s = 0$. The description is in mathematical terms, but is analogous to what could be done experimentally. The first step in this method is adjustment of the temperature in order to achieve phase matching for the specified frequency. This is just a matter of changing the temperature to the value determined by Eq. (21). Next the pump frequency and the temperature are adjusted simultaneously in order to maintain the $\Delta k = 0$ phase-matching condition and to satisfy the condition $\Delta m = 0$. Numerically this is done by setting $\Delta k = 0$ and $\Delta m = 0$ in Eqs. (21) and (22) and solving for $T$ and $\omega_p$ with $V$ and $\omega_s$ held constant. Next, three parameters are adjusted simultaneously by solving Eqs. (21)–(23) for $T$, $\omega_p$, and $V$ with $\omega_s$ again held constant and $\Delta k$, $\Delta m$, and $\Delta m_s$ set to zero.

In practice this mathematical procedure would be analogous to setting temperature to a value calculated for phase matching and observing the location of the cluster curve nearest the phase-matched signal frequency. Next, the temperature and the pump frequency are adjusted simultaneously in order to move that cluster curve to intersect the desired frequency at phase matching. At this point oscillation is on the resonance nearest the specified frequency. Finally the temperature, the pump frequency, and the voltage are adjusted simultaneous in order to bring the cavity resonance to the desired frequency while maintaining coincidence of the signal and the idler modes and phase matching.

The second method of three-parameter tuning concerns a situation in which oscillation is achieved with optimum phase matching and coincidence of the modes in satisfying the conservation-of-energy condition. Continuous output frequency tuning is possible over a limited range while optimum DRO operating conditions are maintained. One parameter can be changed arbitrarily, but the other parameters must be changed in a prescribed manner. The prescription for this change is again obtained by differentiating Eqs. (21)–(23) and this time setting all total derivatives equal to zero. The pump frequency $\omega_p$ is chosen as the independent parameter, and the differentiation yields

$$\frac{d\Delta k}{d\omega_p} = 0 = \left(\frac{\partial \Delta k}{\partial \omega_s}\right)_{\omega_p} \frac{d\omega_s}{d\omega_p} + \left(\frac{\partial \Delta k}{\partial \omega_p}\right)_{\omega_s} + \frac{\partial \Delta k}{\partial T}\frac{dT}{d\omega_p} + \frac{\partial \Delta k}{\partial V}\frac{dV}{d\omega_p}, \tag{43a}$$

$$\frac{dm}{d\omega_p} = 0 = \left(\frac{\partial m}{\partial \omega_s}\right)_{\omega_p} \frac{d\omega_s}{d\omega_p} + \left(\frac{\partial m}{\partial \omega_p}\right)_{\omega_s} + \frac{\partial m}{\partial T}\frac{dT}{d\omega_p} + \frac{\partial m}{\partial V}\frac{dV}{d\omega_p}, \tag{43b}$$

and

$$\frac{dm_s}{d\omega_p} = 0 = \frac{\partial m_s}{\partial \omega_s}\frac{d\omega_s}{d\omega_p} + \frac{\partial m_s}{\partial \omega_p} + \frac{\partial m_s}{\partial T}\frac{dT}{d\omega_p} + \frac{\partial m_s}{\partial V}\frac{dV}{d\omega_p}. \tag{43c}$$

Again, only the first partial derivatives, evaluated in the region of consideration, are required. All of the partial derivatives are determined by material characteristics and the DRO configuration, resulting in three linear equations with three unknowns, which are solved by the usual methods. Continuous frequency coverage can be obtained with an incremental series of continuous frequency sweeps. A calculation of tuning in this manner is shown in Fig. 19. The extent of tuning for the individual sections will be limited by the range of parameter adjustment. For example, there may be a maximum voltage that can be applied, or the extent of pump frequency tuning may be limited. A limit of ±1000 V was used in Fig. 19.

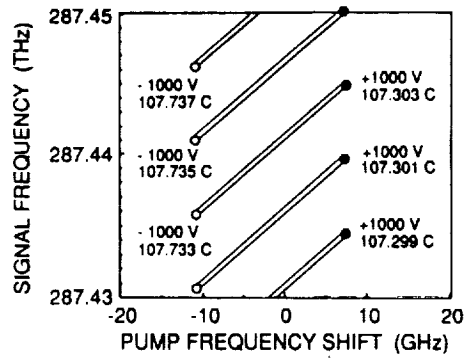


Fig. 19. Calculated tuning for varying the voltage, the pump frequency, and the temperature simultaneously so as to maintain $\Delta m = 0$, $\Delta m_s = 0$, and $\Delta k = 0$.

The calculations of two- and three-parameter tuning show that a DRO can be tuned to any frequency in its operating range[3] with reasonable adjustment of the tuning parameters. Continuous tuning is possible over spectral ranges of approximately the extent of a free spectral range. Complete coverage of larger spectral regions has to be done by scanning a series of smaller regions. The control of individual parameters, particularly temperature, requires difficult tolerances. The control problem can be shifted to another, more easily controlled parameter, such as voltage with multiple-parameter control of the DRO. The degree of correction required on the second parameter can then be used as an error signal for control of the first parameter. Fortunately the oscillating frequencies of the monolithic DRO, exclusive of mode hops, are relatively insensitive to voltage and temperature changes. If mode hops and cluster jumps are avoided, the frequency change of the DRO is approximately one half the frequency change of the pump.

## 5. SUMMARY

The theory that is used to model tuning of the DRO is verified at many stages. The first-order threshold approximation agrees well with more general calculations in the limit of low cavity loss. The theory accurately models observed cluster curves for two monolithic MgO:$LiNbO_3$ DRO's. The modeling includes temperature-dependent dispersion, thermal expansion, and the electro-optic and piezoelectric effects in the nonlinear material. The effect of DRO cavity finesse on the fine details of tuning gives a reasonable explanation of observed cluster jumps. Further substantiation of the model in the fine details of tuning is provided by the accurate prediction of the axial-mode-hop rate for tuning-parameter change.

An understanding of DRO tuning is important for controlled stable operation. Continuous tuning rates were calculated for single- and multiple-parameter adjustment.

Tolerances for stable operation were estimated. The results of these calculations will be useful for DRO design optimization. Multiple-parameter tuning, including pump-frequency adjustment, will be necessary for reaching any arbitrary frequency in the OPO operating range. With appropriate control the DRO will be able to produce stable outputs with a frequency stability as good as that available in the pump source.

The DRO should find application in the generation of stable fixed-frequency radiation. Incremental tuning in controlled mode hops or cluster jumps will have applications in spectroscopy and differential absorption lidar (light detection and ranging). Slow, high-resolution tuning will be possible over limited frequency ranges for spectroscopic applications.

The theory presented here could easily be extended to DRO configurations other than monolithic devices. Other degrees of freedom, such as direct length control in a discrete-component DRO, would provide greater versatility in operation. Independent control of signal and idler cavity lengths would be useful in providing greatly extended ranges of continuous tuning. The development of stable DRO operation is now possible through the combination of improved nonlinear-optical materials and frequency-stable laser development, such as in diode-pumped solid-state lasers. Optical parametric oscillators again appear to be on the threshold of reaching a potential that was first understood twenty-five years ago.

## APPENDIX A. MATERIAL PROPERTIES OF MgO:LiNbO$_3$ RELATED TO DRO TUNING

### A. Temperature-Dependent Dispersion

Edwards and Lawrence[26] developed temperature-dependent dispersion equations for congruently grown $LiNbO_3$, based on data reported by Nelson and Mikulyak[27] and Smith *et al.*[28] They use dispersion equations of the form

$$n^2 = A_1 + \frac{A_2 + B_1 F}{\lambda^2 - (A_3 - B_2 F)^2} + B_3 F - A_4 \lambda^2, \quad \text{(A1)}$$

where

$$F = (T - T_0)(T + T_0 + 546), \quad \text{(A2)}$$

$\lambda$ is wavelength in micrometers, and $T$ is temperature in degrees Celsius. Coefficients for congruent $LiNbO_3$ are as follows:

| | Ordinary | Extraordinary |
|---|---|---|
| $A_1$ | 4.9048 | 4.5820 |
| $A_2$ | 0.11775 | 0.09921 |
| $A_3$ | 0.21802 | 0.21090 |
| $A_4$ | 0.027153 | 0.021940 |
| $B_1$ | $2.2314 \times 10^{-8}$ | $5.2716 \times 10^{-8}$ |
| $B_2$ | $-2.9671 \times 10^{-8}$ | $-4.9143 \times 10^{-8}$ |
| $B_3$ | $2.1429 \times 10^{-8}$ | $2.2971 \times 10^{-7}$ |
| $T_0$ | 24.5 | 24.5 |

The material used in this work is not congruent $LiNbO_3$; rather, it is 5%MgO:$LiNbO_3$. There is little refractometric data available this material. To obtain an approximate set of equations for 5%MgO:$LiNbO_3$, the extraordinary index was adjusted by changing $A_{1E}$ from 4.5820 to 4.55207. This has the effect of increasing the calculated noncritical phase-matching temperature for 1064–532-nm second-harmonic generation from −19.4 to 107.04°C. The measured value for the MgO-doped material is 107°C.[29] This modification to the congruent dispersion equations accurately reproduces the observed tuning curve for a singly resonant OPO that was tuned between 0.85 and 1.48 $\mu$m by varying temperature between 122 and 190°C.[30] This modification also predicts parametric florescence pumped at 514.5 and 488 nm when the crystal is tuned between 100 and 450°C (Table A1).

### B. Electro-Optic Effect

Electro-optical, piezoelectric, and thermal expansion characterizations of $LiNbO_3$ are reviewed by Räuber.[31] A somewhat more extensive tabulation of electro-optical coefficient measurements is given by Yariv and Yeh.[32] Their treatment of the electro-optical effect is followed here. The index ellipsoid in a principle coordinate system is given by

$$\frac{x^2}{n_x^2} + \frac{y^2}{n_y^2} + \frac{z^2}{n_z^2} = 1. \quad \text{(A3)}$$

When an electric field is applied, the electro-optical effect is described by the modified index ellipsoid

$$\left(\frac{1}{n_x^2} + r_{1k}E_k\right)x^2 + \left(\frac{1}{n_y^2} + r_{2k}E_k\right)y^2 + \left(\frac{1}{n_z^2} + r_{3k}E_k\right)z^2 + 2r_{4k}E_k yz + 2r_{5k}E_k xz + 2r_{6k}E_k xy = 1, \quad \text{(A4)}$$

where

**Table A1. Comparison of Measured and Calculated Values for Parametric Fluorescence in MgO:LiNbO$_3$**

| 514.5-nm Pump Wavelength | | | 488-nm Pump Wavelength | |
|---|---|---|---|---|
| Experimental Temperature Setting (°C) | Obs. Fluorescence Wavelength (nm) | Calc. Temperature (°C) | Obs. Fluorescence Wavelength (nm) | Calc. Temperature (°C) |
| 148 | 777.1 | 146.70 | 673.3 | 143.17 |
| 198 | 741.2 | 196.21 | 653.1 | 194.93 |
| 248 | 710.8 | 245.26 | 634.5 | 245.18 |
| 298 | 684.5 | 293.38 | 617.3 | 294.12 |
| 318 | 674.8 | 312.52 | | |
| 348 | 660.8 | 341.50 | 601.3 | 341.86 |
| 398 | 639.2 | 389.31 | 585.7 | 390.38 |
| 448 | 619.2 | 436.60 | | |

$$r_{ik}E_k = \sum_{k=1}^{3} r_{ik}E_k, \qquad i = 1,\ldots 6.$$

For point group $3m$, to which $LiNbO_3$ belongs, the following relationships apply: $n_x = n_y = n_o$, $n_z = n_e$, and

$$(r_{ik}) = \begin{bmatrix} 0 & -r_{22} & r_{13} \\ 0 & r_{22} & r_{13} \\ 0 & 0 & r_{33} \\ 0 & r_{51} & 0 \\ r_{51} & 0 & 0 \\ -r_{22} & 0 & 0 \end{bmatrix}. \tag{A5}$$

There are only four independent electro-optical coefficients. We consider only application of an electric field along the $y$ axis ($E = E_y$), which further simplifies the index ellipsoid to

$$\left(\frac{1}{n_o^2} - r_{22}E_y\right)x^2 + \left(\frac{1}{n_o^2} + r_{22}E_y\right)y^2 + \frac{z^2}{n_e^2} + 2r_{51}E_y yz = 1. \tag{A6}$$

The presence of the $y$–$z$ cross term shows that the electro-optical effect results in a slight rotation of the principal axes. This is a small effect that accounts for less than 1% of the refractive-index change even at the highest fields that are considered here; therefore this rotation is ignored. For propagation in the $x$ direction we have

$$n_y \approx \left(\frac{1}{n_o^2} + r_{22}E_y\right)^{-1/2} \approx n_o - \frac{n_o^3 r_{22}E_y}{2} \tag{A7}$$

and

$$n_z \approx n_e.$$

Yariv and Yeh[32] list three values for $r_{22}$ of $LiNbO_3$, measured with a low-frequency applied electric field for various optical wavelengths:

$$r_{22}(633\text{ nm}) = 6.8 \times 10^{-12}\text{ m/V},$$
$$r_{22}(1.15\ \mu\text{m}) = 5.4 \times 10^{-12}\text{ m/V},$$
$$r_{22}(3.39\ \mu\text{m}) = 3.1 \times 10^{-12}\text{ m/V}.$$

These values suggest that we use $r_{22} = 5.5 \times 10^{-12}$ m/V near the wavelength 1.06 $\mu$m, the wavelength region at which our 5%MgO:$LiNbO_3$ DRO was operated. The value $6.8 \times 10^{-12}$ m/V is from a measurement reported in 1967.[33] Note that this measurement was made even before the growth of congruent $LiNbO_3$ was reported.[34,35] We are working with an still slightly different material 5%MgO:$LiNbO_3$,[24,25] and caution is required in applying these values.

## C. Thermal Expansion

Thermal expansion measurements to second order in temperature for $LiNbO_3$ are reported by Kim and Smith.[36] They express the fractional change of length with the quadratic function

$$\frac{\Delta l}{l} = \alpha(T - T_R) + \beta(T - T_R)^2, \tag{A8}$$

where $l$ is length, $\Delta l$ is change in length, $T$ is temperature in degrees Celsius and $T_R = 25$°C is a reference temperature. The DRO length is measured along the crystal $x$ axis. One set of coefficients,

$$\alpha_{11} = (1.54 \times 10^{-5})\text{°C}^{-1}$$

and

$$\beta_{11} = (5.3 \times 10^{-9})\text{°C}^{-2},$$

apply to expansion in the $x$–$y$ plane, and a second set applies to expansion in the $z$ direction. The spread in the measurements reported by Kim and Smith suggests an accuracy of ~10% in the two coefficients.

## D. Piezoelectric Effect

The direct piezoelectric effect describes the electric polarization $P$ that results when a stress $T$ is applied to a material by the relationship

$$P_i = d_{ijk}T_{jk}, \tag{A9}$$

where $d_{ijk}$ are the piezoelectric moduli. The converse piezoelectric effect describes the strain $S$ that results when an electric field is applied to a piezoelectric material by the relationship[37]

$$S_{jk} = d_{ijk}E_i. \tag{A10}$$

Summation of the repeated indices is implied in both of the above equations, and the moduli $d_{ijk}$ are the same in both equations. The elongation of the DRO cavity is given by $S_{11}$, the $x$ component of the change of a vector that lies in the $x$ direction. For these measurements an electric field is applied in the $y$ direction, $E_y$, and the modulus $d_{211}$ is required for the calculation of strain. The symmetry of the stress tensor permits the use of a contracted subscript notation in which the modulus $d_{211}$ is expressed as $d_{21}$. The $3m$ symmetry of the lithium niobate crystal reduces the number of independent moduli to four. The reduced matrix of piezoelectric moduli for the point group $3m$ is

$$(d_{jm}) = \begin{bmatrix} 0 & 0 & 0 & 0 & d_{15} & -2d_{22} \\ -d_{22} & d_{22} & 0 & d_{15} & 0 & 0 \\ d_{31} & d_{31} & d_{33} & 0 & 0 & 0 \end{bmatrix}. \tag{A11}$$

From the relationships between the moduli, it follows that strain is given by

$$S_{11} = d_{211}E_2 = d_{21}E_2 = -d_{22}E_y. \tag{A12}$$

The value of the piezoelectric modulus reported by Smith and Welsh,[38] $d_{22} = (2.08 \times 10^{-11})$ C/N, is used. They identify the $LiNbO_3$, which they used as commercially grown, with a Curie point of 1165°C. Sound-propagation measurements were used to determine the piezoelectric moduli.

The derivatives used in Eqs. (21)–(23) are expanded in Eqs. (18) and Table 1. Evaluation for the experimental conditions described in Section 3 with the material properties described above is given in Table 2. Derivatives involving the electro-optic and the piezoelectric effects

are given with respect to the voltage applied to the electrodes on the crystal surfaces perpendicular to the $y$ axis. An effective crystal thickness between the electrodes, $t$, is used, and the derivatives are given by

$$\frac{\partial \Delta k}{\partial V} = (\omega_s n_s^3 + \omega_i n_i^3)\frac{r_{22}}{2ct}, \tag{A13}$$

$$\frac{\partial m}{\partial V} = -\frac{l}{\pi ct}\left[(n_s\omega_s + n_i\omega_i)d_{22} + (\omega_s n_s^3 + \omega_i n_i^3)\frac{r_{22}}{2}\right], \tag{A14}$$

and

$$\frac{\partial m_s}{\partial V} = -\frac{l}{\pi ct}\left(n_s\omega_s d_{22} + \omega_s n_s^3\frac{r_{22}}{2}\right). \tag{A15}$$

## ACKNOWLEDGMENTS

This work was supported by the Office of Naval Research through contracts N00014-88-K-0576 and N00014-88-K-0701 and by NASA through grant NAGW-1760. C. D. Nabors and W. J. Kozlovsky are grateful to the Fannie and John Hertz Foundation for support of their graduate studies. We express our appreciation to Crystal Technology of Palo Alto, California, for supplying the MgO:$LiNbO_3$ material. Our appreciation is also extended to many individuals who helped in a number of ways. Martin Fejer and Eric Gustafson provided many helpful discussions and suggestions in the course of this work. Dieter Jundt performed the parametric fluorescence measurements of phase matching for MgO:$LiNbO_3$. Stephen Yang operated the apparatus for the measurements shown in Fig. 10. The help of Janet Okagaki in formating and preparing the figures and the optical fabrication of the monolithic DRO's by Joe Vrhel are especially appreciated.

*note added in proof*

The tuning properties of doubly resonant oscillation in waveguide OPO's have been observed by Suche and Sohler.[39] There are many similarities between the tuning properties described here and those reported for the waveguide cavities. Piskarskas *et al.*[40] have reported cluster effects in the output of DRO's synchronously pumped by cw mode-locked laser output. Wong[41] has proposed the use of DRO's for optical frequency synthesis. The increased photoconductivity and the trapping of charges in MgO:$LiNbO_3$ may pose some problems in the use of dc electric fields with that material.[25]

*Present address, MIT Lincoln Laboratory, 244 Wood Street, Lexington, Massachusetts 02173.

†Present address, IBM Almden Research Center, 650 Harry Road, San Jose, California 95120.

## REFERENCES

1. J. A. Giordmaine and R. C. Miller, "Tunable coherent parametric oscillation in $LiNbO_3$ at optical frequencies," Phys. Rev. Lett. **14**, 973–976 (1965).
2. J. A. Giordmaine and R. C. Miller, "Optical parametric oscillation in $LiNbO_3$," in *Physics of Quantum Electronics*, P. L. Kelley, B. Lax, and P. E. Tannenwald, eds. (McGraw, New York, 1966), pp. 31–42.
3. G. D. Boyd and A. Ashkin, "Theory of parametric oscillator threshold with single-mode optical masers and observation of amplification in $LiNbO_3$," Phys. Rev. **146**, 187–198 (1966).
4. R. G. Smith, "A study of factors affecting the performance of a continuously pumped doubly resonant optical parametric oscillator," IEEE J. Quantum Electron. **QE-9**, 530–541 (1973).
5. S. E. Harris, "Tunable optical parametric oscillators," Proc. IEEE **57**, 2096–2113 (1969).
6. R. G. Smith, "Optical parametric oscillators," in *Advances in Lasers*, A. K. Levine and A. J. DeMaria, eds. (Dekker, New York, 1976), Vol. 4, pp. 189–307.
7. R. L. Byer, "Parametric oscillators and nonlinear materials," in *Nonlinear Optics*, P. G. Harper and B. S. Wherrett, eds. (Academic, San Francisco, 1977), pp. 47–160; R. L. Byer, "Optical parametric oscillators," in *Quantum Electronics: A Treatise*, H. Rabin and C. L. Tang, eds. (Academic, New York, 1975), Vol. 1, part B, pp. 587–702.
8. For example, see A. Yariv, *Quantum Electronics*, 3rd. ed. (Wiley, New York, 1989), Chap. 17, or Y. R. Shen, *The Principles of Nonlinear Optics* (Wiley, New York, 1984), Chap. 9.
9. R. Graham and H. Haken, "The quantum-fluctuations of the optical parametric oscillator. I," Z. Phys. **210**, pp. 276–302 (1968).
10. C. D. Nabors, S. T. Yang, T. Day, and R. L. Byer, "Coherence properties of a doubly resonant monolithic optical parametric oscillator," J. Opt. Soc. Am. B. **7**, 815–820 (1990).
11. J. E. Bjorkholm, "Analysis of the doubly resonant optical parametric oscillator without power-dependent reflections," IEEE J. Quantum Electron. **QE-5**, 293–295 (1969).
12. J. Falk, "Instabilities in the doubly resonant parametric oscillator: a theoretical analysis," IEEE J. Quantum Electron. **QE-7**, 230–235 (1971).
13. J. A. Armstrong, N. Bloembergen, J. Ducuing, and S. Pershan, "Interactions between light waves in a nonlinear dielectric," Phys. Rev. **127**, 1918–1939 (1962).
14. M. Born and E. Wolf, *Principles of Optics*, 3rd ed. (Pergamon, Oxford, 1965), pp. 323–329.
15. A. Siegman, *Lasers* (University Science, Mill Valley, Calif., 1986), pp. 435–436.
16. G. D. Boyd and D. A. Kleinman, "Parametric interaction of focused Gaussian light beams," J. Appl. Phys. **39**, 3597–3639 (1968).
17. W. J. Kozlovsky, C. D. Nabors, R. C. Eckardt, and R. L. Byer, "Monolithic MgO:$LiNbO_3$ doubly resonant optical parametric oscillator pumped by a frequency-doubled diode-laser-pumped Nd:YAG laser," Opt. Lett. **14**, 66–68 (1989).
18. C. D. Nabors, R. C. Eckardt, W. J. Kozlovsky, and R. L. Byer, "Efficient single-axial-mode operation of a monolithic MgO:$LiNbO_3$ optical parametric oscillator," Opt. Lett. **14**, 1134–1136 (1989).
19. T. Kane and R. L. Byer, "Monolithic, unidirectional, single-mode Nd:YAG ring laser," Opt. Lett. **10**, 65–67 (1985).
20. A. Nilsson, E. Gustafson, and R. L. Byer, "Eigenpolarization theory of monolithic nonplanar ring oscillators," IEEE J. Quantum Electron. **25**, 767–790 (1989).
21. W. J. Kozlovsky, C. D. Nabors, and R. L. Byer, "Efficient second harmonic generation of a diode-laser-pumped cw Nd:YAG laser using monolithic MgO:$LiNbO_3$ external resonant cavities," IEEE J. Quantum Electron. **24**, 913–919 (1988).
22. B.-K. Zhou, T. J. Kane, G. J. Dixon, and R. L. Byer, "Efficient, frequency-stable laser-diode-pumped Nd:YAG lasers," Opt. Lett. **10**, pp. 62–64 (1985).
23. T. J. Kane, A. C. Nilsson, and R. L. Byer, "Frequency stability and offset locking of a laser-diode-pumped Nd:YAG monolithic nonplanar ring oscillator," Opt. Lett. **12**, 175–177 (1987).
24. G.-G. Zhong, L. Jian, and Z.-K. Wu, *Eleventh International Quantum Electronics Conference* (IEEE, New York, 1980), p. 631.
25. D. A. Bryan, R. R. Rice, R. Gerson, H. E. Tomaschke, K. L. Sweeney, and L. E. Halliburton, "Magnesium-doped lithium niobate for higher optical power applications," Opt. Eng. **24**, 138–143 (1985).

26. G. J. Edwards and M. Lawrence, "A temperature-dependent dispersion equation for congruently grown lithium niobate," Opt. Quantum Electron. **16**, 373–375 (1984).
27. D. F. Nelson and R. M. Mikulyak, "Refractive indices of congruently melting lithium niobate," J. Appl. Phys. **45**, 3688–3689 (1974).
28. D. S. Smith, H. D. Riccius, and R. P. Edwin, "Refractive indices of lithium niobate," Opt. Commun. **17**, 332–335 (1976); errata, **20**, 188 (1977).
29. J. L. Nightingale, W. J. Silva, G. E. Reade, A. Rybicki, W. J. Kozlovsky, and R. L. Byer, "Fifty percent conversion efficiency second harmonic generation in magnesium oxide doped lithium niobate," Proc. Soc. Photo-Opt. Instrum. Eng. **681**, 20–24 (1986).
30. W. J. Kozlovsky, E. K. Gustafson, R. C. Eckardt, and R. L. Byer, "OPO performance with a long pulse length, single frequency Nd:YAG laser pump," Proc. Soc. Photo-Opt. Instrum. Eng. **912**, 50–53 (1988).
31. A. Räuber, "Chemistry and physics of lithium niobate," in *Current Topics in Materials Science*, E. Kaldis, ed. (North-Holland, Amsterdam, 1978), Vol. 1, pp. 481–601.
32. A. Yariv and P. Yeh, *Optical Waves in Crystals* (Wiley, New York, 1984), chap. 7.
33. J. D. Zook, D. Chen, and G. N. Otto, "Temperature dependence and model of the electro-optic effect in $LiNbO_3$," Appl. Phys. Lett. **11**, 159–161 (1967).
34. R. L. Byer, J. F. Young, and R. S. Feigelson, "Growth of high-quality $LiNbO_3$ crystals from the congruent melt," J. Appl. Phys. **41**, 2320 (1970).
35. F. R. Nash, G. D. Boyd, M. Sargent III, and P. M. Bridenbaugh, "Effect of optical inhomogeneities on phase matching in nonlinear crystals," J. Appl. Phys. **41**, 2564–2575 (1970).
36. Y. S. Kim and R. T. Smith, "Thermal expansion of lithium tantalate and lithium niobate single crystals," J. Appl. Phys. **40**, 4637–4641 (1969).
37. J. F. Nye, *Physical Properties of Crystals* (Oxford, London, 1985), chap. 7.
38. R. T. Smith and F. S. Welsh, "Temperature dependence of the elastic, piezoelectric, and dielectric constants of lithium tantalate and lithium niobate," J. Appl. Phys. **42**, 2219–2230 (1971).
39. H. Suche and W. Sohler, "Integrated optical parametric oscillators," Optoelectronics–Devices and Technologies (Tokyo) **4**, 1–20, (1989).
40. A. Piskarskas, V. Smil'gyavichyus, and A, Umbrasas, "Continuous parametric generation of picosecond light pulses," Sov. J. Quantum Electron. **18**, 155-156 (1988).
41. N. C. Wong, "Optical frequency division using an optical parametric oscillator," Opt. Lett. **15**, 1129–1131 (1990).